The Astrophysical Journal, 916:12 (19pp), 2021 July 20 https://doi.org/10.3847/1538-4357/ac01d7

Measuring the Average Molecular Gas Content of Star-forming Galaxies at $z = 3$–4

Leindert A. Boogaard[1], Rychard J. Bouwens[1], Dominik Riechers[2,3], Paul van der Werf[1], Roland Bacon[4], Jorryt Matthee[5], Mauro Stefanon[1], Anna Feltre[6], Michael Maseda[1], Hanae Inami[7], Manuel Aravena[8], Jarle Brinchmann[1,9], Chris Carilli[10,11], Thierry Contini[12], Roberto Decarli[6], Jorge González-López[8,13], Themiya Nanayakkara[14], and Fabian Walter[3,10]

[1] Leiden Observatory, Leiden University, PO Box 9513, NL-2300 RA Leiden, The Netherlands; boogaard@strw.leidenuniv.nl
[2] Cornell University, 220 Space Sciences Building, Ithaca, NY 14853, USA
[3] Max Planck Institute für Astronomie, Königstuhl 17, D-69117 Heidelberg, Germany
[4] Univ. Lyon 1, ENS de Lyon, CNRS, Centre de Recherche Astrophysique de Lyon (CRAL) UMR5574, F-69230 Saint-Genis-Laval, France
[5] Department of Physics, ETH Zurich, Wolfgang-Pauli-Strasse 27, 8093, Zurich, Switzerland
[6] INAF-Osservatorio di Astrofisica e Scienza dello Spazio, via Gobetti 93/3, I-40129, Bologna, Italy
[7] Hiroshima Astrophysical Science Center, Hiroshima University, 1-3-1 Kagamiyama, Higashi-Hiroshima, Hiroshima, 739-8526, Japan
[8] Núcleo de Astronomía de la Facultad de Ingeniería y Ciencias, Universidad Diego Portales, Av. Ejército Libertador 441, Santiago, Chile
[9] Instituto de Astrofísica e Ciências do Espaço, Universidade do Porto, CAUP, Rua das Estrelas, PT4150-762 Porto, Portugal
[10] National Radio Astronomy Observatory, Pete V. Domenici Array Science Center, P.O. Box O, Socorro, NM 87801, USA
[11] Battcock Centre for Experimental Astrophysics, Cavendish Laboratory, Cambridge CB3 0HE, UK
[12] Institut de Recherche en Astrophysique et Planétologie (IRAP), Université de Toulouse, CNRS, UPS, F-31400 Toulouse, France
[13] Instituto de Astrofísica, Facultad de Física, Pontificia Universidad Católica de Chile Av. Vicuña Mackenna 4860, 782-0436 Macul, Santiago, Chile
[14] Centre for Astrophysics and Supercomputing, Swinburne University of Technology, Hawthorn, VIC 3122, Australia
Received 2020 October 23; revised 2021 May 12; accepted 2021 May 13; published 2021 July 20

Abstract

We study the molecular gas content of 24 star-forming galaxies at $z = 3$–4, with a median stellar mass of $10^{9.1}\,M_{\odot}$, from the MUSE Hubble Ultra Deep Field (HUDF) Survey. Selected by their Lyα λ1216 emission and $H_{\rm F160W}$-band magnitude, the galaxies show an average $\langle {\rm EW}^{0}_{{\rm Ly}\alpha} \rangle \approx 20$ Å, below the typical selection threshold for Lyα emitters (${\rm EW}^{0}_{{\rm Ly}\alpha} > 25$ Å), and a rest-frame UV spectrum similar to Lyman-break galaxies. We use rest-frame optical spectroscopy from KMOS and MOSFIRE, and the UV features observed with MUSE, to determine the systemic redshifts, which are offset from Lyα by $\langle \Delta v({\rm Ly}\alpha) \rangle = 346$ km s^{-1}, with a 100 to 600 km s^{-1} range. Stacking ^{12}CO $J = 4 \rightarrow 3$ and [C I]^{3}P$_1 \rightarrow {}^3$P$_0$ (and higher-J CO lines) from the ALMA Spectroscopic Survey of the HUDF, we determine 3σ upper limits on the line luminosities of 4.0×10^8 K km s^{-1}pc^2 and 5.6×10^8 K km s^{-1}pc^2, respectively (for a 300 km s^{-1} line width). Stacking the 1.2 mm and 3 mm dust-continuum flux densities, we find a 3σ upper limits of 9 μJy and 1.2 μJy, respectively. The inferred gas fractions, under the assumption of a "Galactic" CO-to-H$_2$ conversion factor and gas-to-dust ratio, are in tension with previously determined scaling relations. This implies a substantially higher $\alpha_{\rm CO} \geqslant 10$ and $\delta_{\rm GDR} \geqslant 1200$, consistent with the subsolar metallicity estimated for these galaxies ($12 + \log({\rm O/H}) \approx 7.8 \pm 0.2$). The low metallicity of $z \geqslant 3$ star-forming galaxies may thus make it very challenging to unveil their cold gas through CO or dust emission, warranting further exploration of alternative tracers, such as [C II].

Unified Astronomy Thesaurus concepts: Molecular gas (1073); High-redshift galaxies (734); Interstellar medium (847); CO line emission (262); Dust continuum emission (412); Spectroscopy (1558)

1. Introduction

The recent decade has witnessed a tremendous advance in the characterization of the cold molecular gas content of star-forming galaxies at $z > 1$. Evidence is now mounting that the cold gas fraction of massive star-forming galaxies strongly increases up to at least $z \approx 3$ (e.g., Genzel et al. 2010, 2015; Tacconi et al. 2010, 2013, 2018; Geach et al. 2011; Dessauges-Zavadsky et al. 2015, 2020; Aravena et al. 2019, 2020; Tacconi et al. 2020). As the cold H_2 gas itself is radiatively dark, the molecular gas has to be traced by the emission from the ground-state rotational transition of carbon monoxide (^{12}CO, hereafter CO), or other tracers such as the emission from neutral atomic carbon ([C I]) or the long-wavelength dust continuum. Yet, observations of CO in (optically selected) star-forming galaxies at $z > 3$ remain challenging and have been limited to massive Lyman-break- or main-sequence-selected galaxies and/or strongly lensed systems, with known redshifts (Baker et al. 2004; Coppin et al. 2007; Riechers et al. 2010; Livermore et al. 2012; Magdis et al. 2012, 2017; Tan et al. 2013; Saintonge et al. 2013; Dessauges-Zavadsky et al. 2015, 2017; Pavesi et al. 2019; Cassata et al. 2020), sometimes serendipitously detected and only identified as such a posteriori (Gowardhan et al. 2019).

The Atacama Large Millimeter Array Large Program ASPECS (The ALMA Spectroscopic Survey in the Hubble Ultra Deep Field (HUDF); Walter et al. 2016; Decarli et al. 2019) provides a unique opportunity to study the gas content of star-forming galaxies at $z \geqslant 3$. ASPECS consists of spectral scans in ALMA Bands 3 (85–115 GHz) and 6 (212–272 GHz), probing molecular gas and dust in galaxies without any target preselection. These data unveil emission from CO, [C I], and dust continuum in several star-forming galaxies at $z = 1$–4 (Boogaard et al. 2019, 2020; González-López et al. 2019, 2020), providing key constraints on the empirical scaling relations describing the evolution of the gas and dust content in galaxies (Aravena et al. 2019, 2020), the evolution of the cosmic molecular gas density (Decarli et al. 2019, 2020), and the baryon cycle (Walter et al. 2020).

Key to the exploration of the ASPECS data are the large number of spectroscopic redshifts provided by the Multi Unit

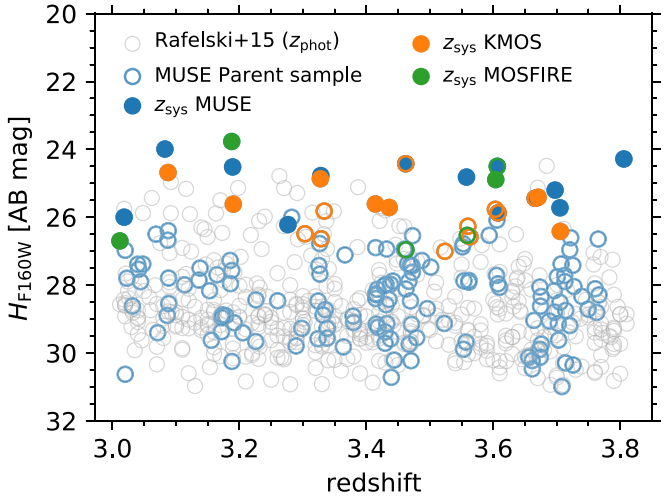

Figure 1. The H_{F160W}-band magnitude of the galaxies considered in this paper as a function of redshift. The open circles show the parent sample of all galaxies with $3.0115 \leqslant z < 3.812$ within the ASPECS field ($\geqslant$40% of the primary beam peak sensitivity) that have a MUSE redshift (from Lyα λ1216) in blue, while the gray circles show all galaxies in the same field with a photometric redshift (Rafelski et al. 2015). Galaxies targeted for KMOS or MOSFIRE follow-up are shown in orange and green, respectively. The filled circles show galaxies for which we obtained a systemic redshift measurement from MUSE (blue), KMOS (orange), or MOSFIRE (green).

Spectroscopic Explorer (MUSE) HUDF Survey (Bacon et al. 2017). Through its unparalleled sensitivity for faint emission lines, MUSE is very efficient in detecting galaxies at $z \geqslant 3$, where the bright H I Lyα λ1216 line enters the integral-field spectrograph (4750–9300 Å; $\lambda/\Delta\lambda \approx 3000$; Inami et al. 2017), probing the faint end of the Lyα luminosity function down to below 0.1 $L^*_{\rm Lya}$ (Drake et al. 2017).

Exploiting the large number of redshifts from MUSE, we can push the gas mass sensitivity of ASPECS at $z \geqslant 3$ to its limits through stacking (in particular, CO $J = 4 \rightarrow 3$ becomes accessible at $z \geqslant 3.0115$). Indeed, Inami et al. (2020) have shown that at lower redshifts, $z = 1$–2, we can recover CO emission below the formal sensitivity threshold of ASPECS by stacking on the accurate systemic redshifts from MUSE.

However, the MUSE redshifts at $z \geqslant 3$ obtained from Lyα cannot be used for stacking. Because Lyα is a resonant transition, the photons are easily scattered by the neutral gas in and surrounding a galaxy, shifting the peak of the emission away from the systemic velocity by several hundred km s^{-1} (e.g., Shapley et al. 2003; Verhamme et al. 2018; Muzahid et al. 2020). This means that the line emission tracing the molecular gas could be completely washed out by the noise if nonsystemic Lyα-redshifts are used for stacking.

Fortunately, because we have approximate redshifts from Lyα, these targets can be effectively followed up simultaneously with multiobject, near-infrared spectrographs, such as the K-band Multi Object Spectrograph (KMOS) at the Very Large Telescope and the Multi-Object Spectrometer For Infra-Red Exploration (MOSFIRE) at the Keck Observatory. These data can constrain the systemic redshift by targeting the rest-frame optical lines such as Hβ λ4863 and [O III] $\lambda\lambda$4960, 5008 in the K band (out to $z = 3.812$).

In this paper, we constrain the molecular gas content of star-forming galaxies at $3.0115 < z < 3.812$ by stacking their molecular gas signal through the outlined three-step process. We 1) identify the galaxies from MUSE and 2) determine their systemic redshifts through rest-frame NIR spectroscopy with KMOS/MOSFIRE (as well as rest-UV features from MUSE; Section 2). We then 3) turn to ALMA to stack the CO and [C I] signal from the ASPECS data, as well as the 1.2 mm dust continuum (Section 3). We do not detect any (line) emission in the stacks (at the 3σ level) and discuss the implications of this nondetection on metallicity, the CO-to-H_2 conversion factor ($\alpha_{\rm CO}$), and gas-to-dust ratio ($\delta_{\rm GDR}$) in Section 4. The results highlight that the metallicity evolution of star-forming galaxies makes it increasingly challenging to infer the molecular gas content at higher redshifts, which warrants the further theoretical and observational exploration of alternative tracers, in particular the [C II] λ158 μm line.

Throughout this paper, we report wavelengths in vacuo and magnitudes in the AB system (Oke & Gunn 1983) and adopt a Chabrier (2003) initial mass function. We use log to denote $\log_{10}$ and ln for the natural logarithm. We adopt a concordance cosmology with $H_0 = 70$ km s^{-1} Mpc^{-1}, $\Omega_m = 0.3$, and $\Omega_\Lambda = 0.7$, in good agreement with the measurements from Planck Collaboration et al. (2016).

2. Observations and Sample Selection

2.1. Parent Sample Selection and Physical Properties

We construct a parent sample of galaxies from the MUSE HUDF Survey Data Release 2 catalog,[15] which is an updated and revised version of the DR1 catalog (Bacon et al. 2017; Inami et al. 2017). In short, the catalog contains both emission-line-selected sources (from ORIGIN; Mary et al. 2020) and continuum-selected sources (from the Hubble Space Telescope (HST) catalog by Rafelski et al. 2015) for which the redshifts are determined automatically. These sources have subsequently been verified by several independent groups of experts that inspect the redshift and the multiwavelength counterpart associations, and assign a confidence flag (ZCONF; where confidence $\geqslant$2 implies a secure redshift, determined by at least two spectral features). Specifically, we use the following criteria:

1. Select all objects with $3.0115 < z < 3.812$ and ZCONF $\geqslant 2$ that have an HST counterpart in the Rafelski et al. (2015) catalog.
2. Restrict to objects that lie within the 4.55 arcmin^2 region of the ASPECS Band 3 mosaic where the sensitivity is $\geqslant$ 40% of the primary beam peak sensitivity at 99.5 GHz.[16]
3. Remove three X-ray-detected sources that are classified as having an active galactic nucleus (AGN; MUSE-1051, MUSE-1056, and MUSE-6672), based on the Chandra 7 MS data (Luo et al. 2017).

There are a total of 168 galaxies in the parent sample constructed this way. The H_{F160W} magnitude of the parent sample is shown as a function of redshift in Figure 1. Because of the sensitivity of MUSE to faint emission-line sources, it consists almost exclusively of galaxies that are selected by their Lyα λ1216 emission. Only six galaxies are not marked as such: one is MUSE-50, which does show double-peaked Lyα-emission on top of strong Lyα absorption, as well as strong UV lines. The other five indeed show little Lyα emission: one is a faint C IV $\lambda\lambda$1548, 1551-only emitter, while the other four have

[15] DR2 v0.1; R. Bacon, et al., in preparation

[16] This area fully encompasses the ASPECS Band 6 mosaic.

bright enough UV continuum to have their systemic redshifts determined from absorption lines (see Section 2.2.1).

Because the Lyα emission may peak in the halo of a galaxy, the association of a MUSE source with an HST counterpart can be ambiguous and is typically resolved during the redshift determination process. The associations adopted here are listed in Table 3 and are in all cases supported by a second tracer of the systemic redshift. In the case of MUSE-6518, the photometry is completely blended with a $z = 0.83$ foreground object, and we do not use it to obtain physical properties.

We determine a stellar mass (M_*) and star formation rate (SFR) for all galaxies in the parent sample by fitting 11 bands of HST (Rafelski et al. 2015) and 4 bands of Spitzer/IRAC photometry, using the high-z extension of the spectral energy distribution fitting code MAGPHYS (Da Cunha et al. 2008, 2015). As in Labbé et al. (2006, 2010, 2015), the deblended Spitzer/IRAC photometry was measured with MOPHONGO, using the HST observations as a template, in the deep ~200 hr data from the GREATS program (M. Stefanon et al., submitted). The latter provides constraints on the rest-frame optical part of the spectral energy distribution redward of the 4000 Å break and is critical to pin down the stellar masses of our galaxies. The results are listed in Table 3 for the galaxies in the systemic redshift sample.

As part of the DR2, the spectra of all galaxies are modeled with PYPLATEFIT (R. Bacon, et al., 2021, in preparation), the Python implementation of the spectrum fitting code PLATEFIT, originally developed for the Sloan Digital Sky Survey (Brinchmann et al. 2004, 2008; Tremonti et al. 2004). The most salient features of PYPLATEFIT, relevant to this work, are that it can simultaneously model both the emission and absorption lines, as well as the stellar continuum, allowing for velocity differences between groups of lines (such as Lyα and other UV lines). All lines are modeled using Gaussians except Lyα, for which a (double) asymmetric Gaussian[17] is used (double if the Lyα line is double peaked).

2.2. Measurement of Systemic Redshifts

We obtain systemic redshifts for galaxies in our parent sample from either the rest-frame UV features using MUSE (Section 2.2.1) or the rest-frame optical emission lines with near-IR spectroscopy (Sections 2.2.2 and 2.2.3). For the near-IR follow-up, targets were selected by their $H_{\rm F160W}$ magnitude (as a proxy for stellar mass) and the absence of a systemic redshift from MUSE in the DR1 reductions. Fainter targets were sometimes observed because brighter targets were no longer accessible given the small size of the HUDF and physical limitations in the positioning arms and slits of multiobject spectrographs.

2.2.1. MUSE

For a subset of galaxies we can determine the systemic redshift directly from the MUSE spectra, using the weaker rest-frame UV emission lines, or absorption features. We identify objects in the parent sample that are cataloged as having a signal-to-noise ratio $(S/N) > 3$ in at least one UV emission line. We focus specifically on O III] $\lambda\lambda$1661, 1666; S III] $\lambda\lambda$1883, 1892; C III] $\lambda\lambda$1907, 1909; and a selection of absorption lines[18] that trace the systemic redshift. We also fit narrow He II λ1640 together with the emission lines, finding it at a similar velocity offset as the other UV lines. We do not use the resonant lines, such as C IV $\lambda\lambda$1548, 1551, which can be offset from the systemic velocity like Lyα. To identify absorption-line redshifts, we inspect all objects with $V_{\rm F606W} \leqslant 27$ and/or $i_{\rm F775W} \leqslant 27$, finding that we can determine these in several galaxies down to $i_{\rm F775W} = 26$. We use PYPLATEFIT to fit the selected spectra, performing 200 bootstrap iterations to obtain a more robust estimate of the uncertainties (both on Lyα and the other features). We only keep the objects that remain at $S/N > 3.5$ in at least one emission line or the sum of the absorption features. In addition, we keep MUSE-1360 as a tentative candidate, having both a tentative detection in the KMOS data and an absorption-line redshift at $S/N = 3$. The $z_{\rm Ly\alpha}^{\rm red}$ and $z_{\rm sys}$, with their bootstrapped uncertainties, are provided in Table 3 (where $z_{\rm Ly\alpha}^{\rm red}$ is the redshift of the red peak of Lyα). We note that three of these sources were also part of the study of Lyα velocity offsets by Verhamme et al. (2018).

In principle, one could estimate the systemic redshift by using half of the peak separation for Lyα lines with a blue bump (Verhamme et al. 2018). Indeed, a few galaxies in our sample also show blue-bump emission. However, systematic searches for blue-bump Lyα emitters are still ongoing, and we therefore do not include such a sample at this stage. Furthermore, the presence of a blue bump requires specific radiative transfer conditions, and selecting a sample in such a way may introduce a bias in the stack.

2.2.2. KMOS

The KMOS observations were taken in two ESO periods as part of 099.A-0858(A) (PI: Bouwens) and 0101.A-0725(A) (PI: Boogaard). We used the HK grating (with a spectral resolution of $\lambda/\Delta\lambda \approx 1800$) in five observing blocks (OBs) per period, with an ABA ABA AB sky-offset pattern between the science (A) and sky (B) frames with 300 s integrations and 0.″2 dithering offsets. In total we targeted 17 galaxies, with (final) on-source times ranging between 200 and 250 minutes. We also included a bright quasar on all masks to control the astrometry, from which we measure the image quality to be around 0.″75 and 0.″85 in the reduced P99 and P101 data, respectively.

We reduce the data using ESO KMOS pipeline version `2.1.0` (Davies et al. 2013), using the standard star observations for the zero-point, response, and telluric correction. We enable the `background` flag to correct for differences in the residual background level between the exposures by applying a constant offset, estimated by taking the mode of the pixel values after excluding the brightest 25%. We discard the data from one detector for the second A frame of the first OB in period 99, which shows a strong background offset. We experimented with further reducing the sky-line residuals using the `sky-tweak` and `molecfit` options of the pipeline, but found that these sometimes introduce artifacts in the data. As our lines were selected to be away from the sky lines as much as possible, we therefore do not apply these corrections. Because of the density of the sky lines around [O II] λ3727 in the H band, we focus on the Hβ λ4863 and [O III] $\lambda\lambda$4960,

[17] Also known as the skew normal distribution, $f(x) = 2\phi(x)\Phi(\gamma x)$, where $\phi(x)$ is the standard normal (Gaussian) distribution, $\Phi(x)$ is the cumulative distribution function for a standard normal distribution, and γ is the skewness parameter.

[18] Si II λ1260, O II λ1302, Si II λ1304, C II λ1335, Si IV $\lambda\lambda$1394, 1403, Fe II $\lambda\lambda$1608, 1611, Al II λ1671, and Al II $\lambda\lambda$1854, 1862.

5008 in the K band. We apply radial velocity corrections[19] to shift every reduced A–B frame to the solar system barycentric frame (the mean $\langle v_r \rangle = 17.3$ km s^{-1}).

We correct for positional shifts between the different OBs by centering on the continuum position of the reference quasar, which we model with a 2D Gaussian. As objects were placed on different integral field units between periods, their position relative to the reference quasar changes. We therefore first combine and analyze the data from each period separately. To identify the spatial position of each (emission-line-only) object on its integral field unit in each period, we

(i) extract spectra at the a priori expected position (that is, the quasar position or the center of the cube) using the 2D fit of the reference quasar as a spatial model,
(ii) identify the brightest spectral line, [O III] λ5008, based on the Lyα redshift and determine its central wavelength and line width using a Gaussian fit,
(iii) collapse the cube over the channels with line emission to make a "narrow band" through multiplication with the Gaussian fit along the wavelength axis, and
(iv) identify the spatial position in the narrowband image.

We iterate steps (i)–(iv) until we converge on spatial position. Finally, we combine the data from both periods using the best positions and repeat the same steps to obtain the final spectra.

We conservatively only consider the objects for which we can identify the line(s) in each half of the data separately, which gives strong confidence that the line(s) are not (caused by) sky-line residuals. We exclude one source where the blueshift of the lines relative to Lyα resulted in them being too close to the sky lines to determine the centroid and four more sources where a tentative feature was only seen in one period. In total, we confidently detect the rest-frame optical line(s) in 7/17 galaxies. As an example, we show the MUSE and KMOS spectrum for one of the galaxies in Figure 2. The spectra of the remaining galaxies are shown in Figure 12 in Section A.

Finally, we determine the redshift by simultaneously fitting Gaussians (in vacuo) to the Hβ λ4863 and [O III] $\lambda\lambda$4960, 5008 lines (using LMFIT; Newville et al. 2021). We use the inverse of the error spectrum as weights and subtract a running median continuum from the spectrum prior to the fitting. The resulting redshifts are reported in Table 3.

2.2.3. MOSFIRE

The MOSFIRE observations were taken on the night of 28 November 2018 as part of 2018B_N182 (PI: Riechers). We observed a single K-band mask with 0.″7 slits ($\lambda/\Delta\lambda \approx 3610$). We used an AB dither pattern with 180 s exposures, totaling 108 minutes of exposure time on source, with an average seeing of 0.″7. The data were reduced using the standard MOSFIRE Data Reduction Pipeline (Release 2018),[20] using the neon arc lamps for the wavelength calibration. As our objects generally do not show any continuum, we first manually identify (candidate) emission lines in the rectified, two-dimensional spectra (based on the Lyα redshift). We then optimally extract the one-dimensional spectra using a Gaussian model for the spatial profile. As all data were taken on a single night, we apply the radial velocity correction to the final spectra ($v_r = -9.2$ km s^{-1}).[21]

In total, we detect the rest-frame optical lines in 4/7 of the galaxies on the mask that are part of our parent sample (including MUSE-6518, with blended HST photometry). Their spectra are shown in Figure 12. We measure the redshifts as described in Section 2.2.2 and report the results in Table 3.

2.3. Final Systemic Redshift Sample

In total, we use MUSE, KMOS, and MOSFIRE to obtain systemic redshifts for 24 galaxies, 20 of which are originally identified by their Lyα emission, with an average redshift of $\langle z \rangle = 3.45$. The $H_{\rm F160W}$ magnitude of the final sample is shown in comparison to the MUSE parent sample in Figure 1. We have a systemic redshift for most galaxies in the parent sample down to $H_{\rm F160W} = 26$. Because the parent sample is Lyα selected, this raises the question of how representative our sample is for the broader population of galaxies at these epochs. We therefore compare our (parent) sample to all galaxies at the same redshift and over the same field, from the photometric redshift catalog by Rafelski et al. (2015, updated with the MUSE redshifts) after excluding the X-ray AGNs (Luo et al. 2017, as we did for the parent sample) see Figure 1.

We show a histogram of the physical properties of the galaxies in Figure 3. The median stellar mass and SFR of the sample are $10^{9.1}\,M_\odot$ and $10\,M_\odot$ yr^{-1}. The sample encompasses $\geqslant 50\%$ of the galaxies in the MUSE parent sample in the bins down to $M_* \geqslant 10^9$ $M_\odot$ and SFR $\geqslant 3$ $M_\odot$ yr^{-1} and $\geqslant 20\%$ of the galaxies in the broader photometric catalog, down to the same limits.

Our galaxies are faint Lyα emitters in comparison to narrowband-selected samples. The typical Lyα luminosity of our sample is $L_{\rm Ly\alpha} = 10^{42}$ erg s$^{-1} \approx 0.2\,L^*_{\rm Ly\alpha}$ at $z = 3.5$ (e.g., Ouchi et al. 2008; Drake et al. 2017; Herenz et al. 2019). The average rest-frame equivalent width[22] of our sample, $\langle {\rm EW}^0_{\rm Ly\alpha} \rangle \approx 20$ Å, is also small, especially when considering that $\approx$25 Å is the typical lower limit for the definition of a (narrowband-selected) Lyα emitter (LAE; e.g., Matthee et al. 2016). This is likely due to our selection toward objects that are bright in $H_{\rm F160W}$. As such, our galaxies are not necessarily comparable to the typical sample of LAEs, but arguably more similar to the average population of (low-mass) star-forming galaxies

To illustrate this point, we stack the MUSE spectrum of all the galaxies in our sample, using the systemic redshifts, following Feltre et al. (2020). We perform a median and weighted mean stack after normalizing each of the spectra by the median flux density at 1267–1276 Å (matching Rigby et al. 2018). The result is shown in Figure 4. We compare the composite MUSE spectrum to the average spectrum of $z \sim 3$ Lyman-break Galaxies (LBGs; Shapley et al. 2003), the composite spectrum of 14 strongly lensed, star-forming galaxies at $1.6 < z < 3.6$ from the MEGaSaURA sample (Rigby et al. 2018) and the composite MUSE spectrum of all 220 LAEs at $2.9 < z < 4.6$ from Feltre et al. (2020). The median spectrum of the galaxies in our sample shows significantly

[19] $\lambda' = \lambda\sqrt{(1 + v_r/c)/(1 - v_r/c)}$, where λ' and λ are the corrected and uncorrected wavelengths, respectively, c is the speed of light, and v_r is the radial velocity correction to the solar system barycenter, computed with `astropy.coordinates.SkyCoord.radial_velocity_correction`.

[20] https://github.com/Keck-DataReductionPipelines/MosfireDRP

[21] See footnote 19.

[22] The rest-frame equivalent width is computed by PYPLATEFIT, from the total flux in Lyα (including a possible blue bump) over the modeled continuum flux density at 1216 Å (defined such that a positive value indicates emission).

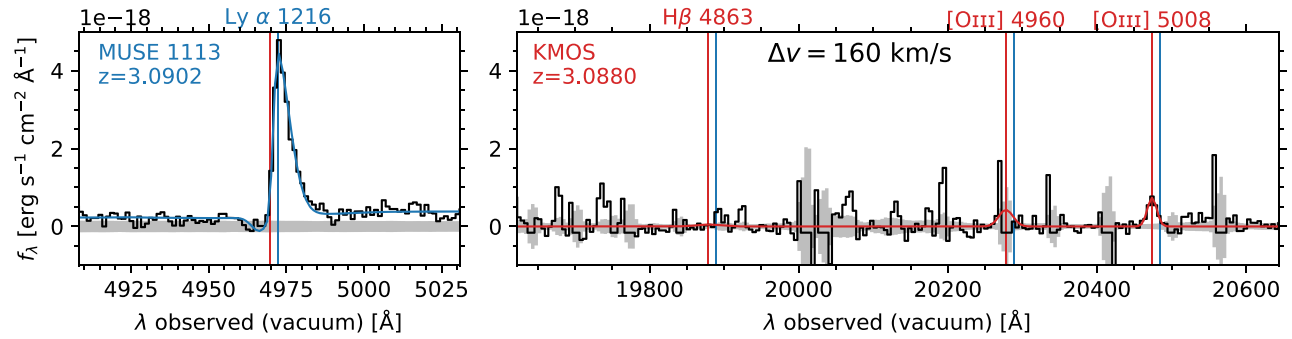

Figure 2. Rest-frame ultraviolet and optical spectra for the first galaxy in the sample with near-infrared follow-up. The left panel shows the MUSE spectrum surrounding the Lyα line. The right panel shows the continuum-subtracted KMOS spectrum around the Hβ λ4863 and [O III] $\lambda\lambda$4960, 5008 lines. In both panels, the vertical blue and red lines indicate the redshift of Lyα and the systemic redshift, respectively, determined from the fit to the spectrum (shown in the same color). This particular galaxy is detected in Lyα λ1216 and [O III] λ5008, but not in Hβ λ4863, showing a positive velocity offset between the red peak of Lyα and the systemic redshift (note [O III] λ4960 falls on top of a sky line). Spectra of the remaining galaxies with KMOS or MOSFIRE observations are shown in Figure 12 in Section A.

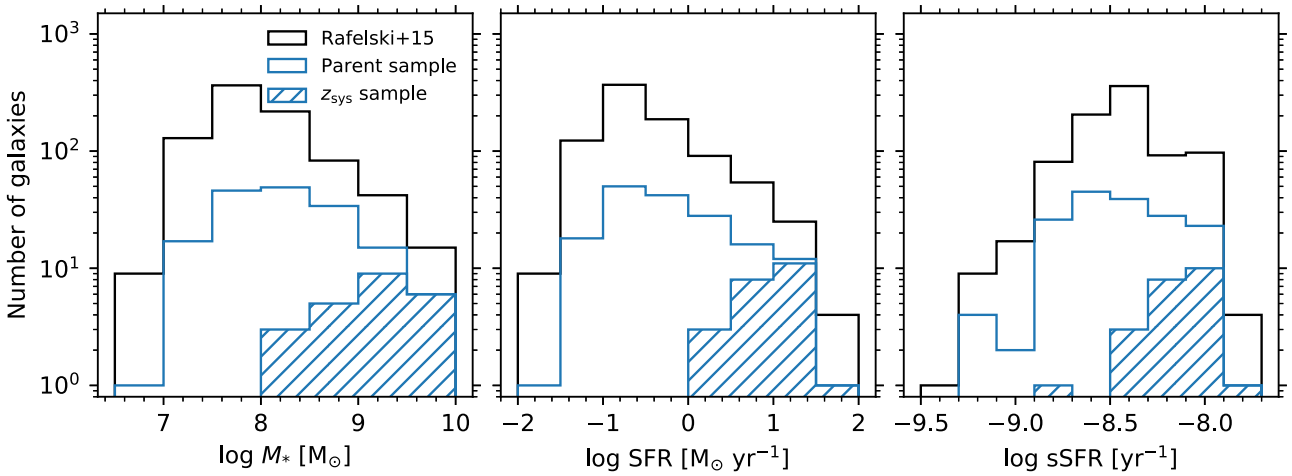

Figure 3. Histograms of the stellar mass (M_*), star formation rate (SFR), and specific SFR (sSFR = SFR/M_*) of the galaxies for which we determine a systemic redshift (z_{sys}), compared to the parent sample from MUSE at $3.0115 \leqslant z < 3.812$ and all galaxies from the photometric redshift catalog by Rafelski et al. (2015).

weaker Lyα emission than the median spectrum of all MUSE LAEs (that includes a majority of LAEs with a fainter $H_{F160W} > 26$). Instead, the similarities in the literature spectra of LBGs and star-forming galaxies and the (median) composite spectrum of our sample support the case that our galaxies are more similar to the population of star-forming galaxies at these epochs.

3. Results

3.1. Velocity Offsets

We plot the velocity offset of Lyα λ1216 with respect to the systemic redshift in Figure 5, defined as $\Delta v(\mathrm{Ly}\alpha) = c(z^{\mathrm{red}}_{\mathrm{Ly}\alpha} - z_{\mathrm{sys}})/(1 + z_{\mathrm{sys}})$, where c is the speed of light. Our galaxies show a mean velocity offset of $\langle \Delta v(\mathrm{Ly}\alpha) \rangle = 346$ km s^{-1}, with a range from 100 to 600 km s^{-1}.

For comparison, the mean $\Delta v(\mathrm{Ly}\alpha) \approx 200$–$250$ km s^{-1} in the LAE samples at $z = 2$–3 (Erb et al. 2014; Trainor et al. 2015), while the $z \sim 3$ LBG sample from Shapley et al. (2003) shows a greater mean velocity offset of 650 km s^{-1}. The relatively large velocity offsets imply a larger H I column density and lower Lyα escape fraction, consistent with the low $\mathrm{EW}^0_{\mathrm{Ly}\alpha}$ of our galaxies (Shapley et al. 2003; Erb et al. 2014; Yang et al. 2017).

The broad distribution in Figure 5 also reflects the smoothing function by which the stacking signal would be diluted if $z^{\mathrm{red}}_{\mathrm{Ly}\alpha}$ would be used for stacking, in particular because the ALMA data has a higher velocity resolution. This highlights the need for systemic redshifts.

3.2. ALMA Stacking

With the systemic redshifts in hand, we turn to the ALMA data. We use the ASPECS Band 3 (Decarli et al. 2019; González-López et al. 2019) and Band 6 (Decarli et al. 2020; González-López et al. 2020) data cubes at their native resolution (≈20 km s^{-1} in both cases). The rms error spectra reach ≈0.2 and 0.5 mJy beam^{-1} channel^{-1} in Band 3 and Band 6, respectively (at the center of the field, varying with frequency).

Before extracting the spectra, we first shift the ALMA cubes from the kinematic local standard of rest to the barycentric frame using the CASA task `imreframe` ($\Delta v = -16.78$ km s^{-1}), such that all our spectroscopic data are on the same velocity frame. We then extract pixel spectra at the HST positions (Rafelski et al. 2015) of our galaxies after correcting for the known astrometric offset ($\Delta\alpha = 0\farcs076$, $\Delta\delta = -0\farcs279$; Dunlop et al. 2017, consistent with Franco et al. 2020). These spectra should contain all the flux as our sources are expected to be unresolved by the ASPECS synthesized beam ($1\farcs8 \times 1\farcs5$ in Band 3 and

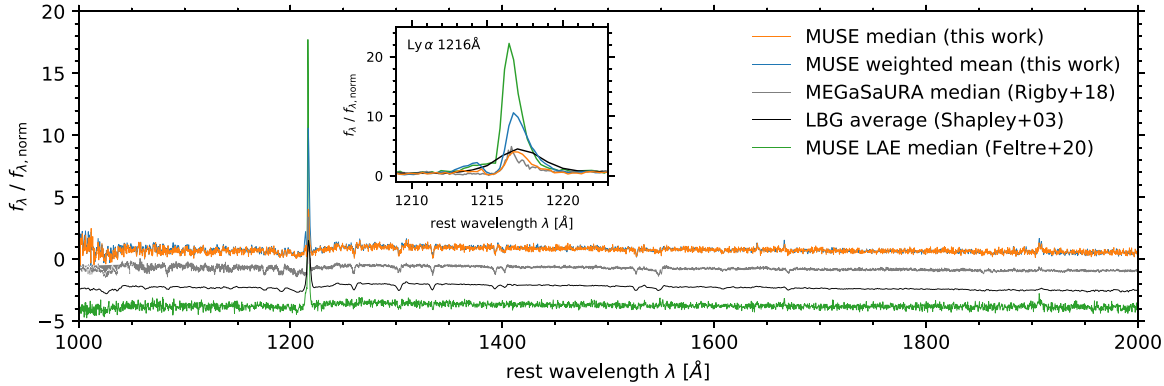

Figure 4. Composite MUSE spectrum of the sample, from both weighted mean (blue) and median (orange) stacking (at 0.3 Å resolution) using the systemic (non-Lyα) redshifts. We compare to the average Lyman-break galaxy (LBG) spectrum at $z \sim 3$ (black) from Shapley et al. (2003, 1 Å resolution) the composite spectrum of 14 strongly lensed, star-forming galaxies at $1.6 < z < 3.6$ from the MEGaSaURA sample (Rigby et al. 2018; the pivot normalized, median stack at 0.1 Å resolution) and the composite MUSE spectrum of all 220 LAEs at $2.9 < z < 4.6$ (Feltre et al. 2020, median stack; note their weighted mean stack is very similar, with slightly stronger Lyα emission). We normalize all spectra to the median flux density at 1267–1276 Å and offset the literature spectra by − 1.5, − 3, and −4.5 for clarity. The inset shows a zoom-in of the Lyα line without vertical offsets. Overall, the composite MUSE spectrum is very similar to the LBGs and MEGaSaURA, showing comparable UV continuum and absorption features, slightly stronger UV emission lines, and a comparable strength of the Lyα line in the median spectrum (notably showing a blue bump). In contrast, the median stack of all LAEs from Feltre et al. (2020) shows significantly stronger Lyα emission, even when compared to the weighted mean spectrum of our galaxies.

$1\farcs5 \times 1\farcs1$ in Band 6). Their spatial extent in the rest-frame UV is significantly smaller, with a median effective radius in H_{F160W} of $\approx 0\farcs2$ (van der Wel et al. 2012).

Inspecting the spectra around the systemic redshift, none of the galaxies are individually detected in their CO or [C I] emission lines at the 3σ level. We therefore stack the spectra as follows (Boogaard et al. 2020; cf. Spilker et al. 2014). We first create a grid in velocity space, centered around zero, with 300 km s^{-1} wide channels. The channel width was chosen based on the mean rest-frame UV/optical line width ($\approx$200 km s^{-1}), such that $> 90\%$ of the stacked line flux is expected to fall within the single central channel. We convert each observed spectrum to velocity space, centered around the line, and bin it onto the velocity grid. We then stack the spectra by taking the $1/\sigma^2$ weighted mean in each velocity channel (where σ is the error) and determine the uncertainty by propagating the error spectrum in the same manner. We finally measure the flux density and the corresponding uncertainty in the zero-velocity channel.

The stacked spectra are shown in Figure 6. None of the lines are detected in the stack at an S/N greater than 3. The stack of CO $J = 9 \rightarrow 8$ shows some signal at the 2σ–3σ level, but we do not consider this a detection. The high-J lines of CO are primarily sensitive to the gas heating (and not the gas mass) and we include the constraints on these lines mainly for completeness and future reference. We compute 3σ upper limits on the integrated line flux, $S_\nu \Delta v$, from the uncertainty in the zero-velocity channel of the stacked spectrum (at 300 km s^{-1} resolution). We determine the corresponding upper limits on the line luminosities via

$$L' = 3.255 \times 10^7\, S_\nu \Delta v\, d_L^2\, \nu_{\mathrm{obs}}^{-2} (1+z)^{-3}\ \mathrm{K\ km\ s^{-1}\ pc^2} \quad (1)$$

(Solomon et al. 1992; Carilli & Walter 2013), adopting the luminosity distance (d_L) and observed frequency (ν_{obs}) at the average redshift of the sample, $z = 3.45$. The results can be found in Table 1. We also perform additional stacks, including only the galaxies with the highest stellar masses ($M_* \geqslant 10^{9.0}$, $\geqslant 10^{9.5}$, and $\geqslant 10^{10}$ $M_\odot$) and the highest star formation rates (SFR $\geqslant 3.2$ and $\geqslant 10$ $M_\odot$ yr^{-1}), but do not obtain any detections. Stacking all the different CO lines together does not yield a detection either (regardless of whether [C I] is also added to this stack).

None of the galaxies are individually detected at the 3σ level in the deep 1.2 mm dust-continuum map (Aravena et al. 2020; González-López et al. 2020). In addition to the line stack, we therefore also perform a weighted mean stack of the 1.2 mm dust-continuum data for the full sample (following the approach from Bouwens 2016; Bouwens et al. 2020, again applying the astrometric offset). We do not obtain a detection, measuring a flux of $S_\nu = 1 \pm 3$ μJy (Figure 7), implying an upper limit of $\leqslant 9$ μJy (3σ). Following the same procedure for the 3 mm continuum results in an upper limit of $\leqslant 1.2$ μJy (3σ). In the following, we focus on the limit from the deep 1.2 mm continuum, as it provides the strongest constraints on the mass in dust and gas.

4. Discussion

4.1. Molecular Gas Masses

Stacking the $\langle z \rangle = 3.45$ star-forming galaxies in the HUDF by their systemic redshifts, we find that $L'_{\mathrm{CO}\,J=4\rightarrow3} \leqslant 4.0 \times 10^8$ K km s^{-1} pc^2. This result puts an upper limit on the molecular gas mass via

$$M_{\mathrm{mol}} = \alpha_{\mathrm{CO}} r_{J1}^{-1} L'_{\mathrm{CO}\,J\rightarrow J-1}, \quad (2)$$

where α_{CO} is known as the CO-to-H_2 conversion factor (a light-to-mass ratio) and r_{J1} is the excitation correction, needed to convert the observed CO luminosity to $L'_{\mathrm{CO}\,J=1\rightarrow0}$. There is no direct measurement of the CO excitation in the galaxies under consideration. Valentino et al. (2020) measured an average $r_{41} = 0.36 \pm 0.06$ in their sample of star-forming galaxies at $z = 1.25$, while Tacconi et al. (2018) assume an average $r_{41} = 0.42$, constant with redshift. Boogaard et al. (2020), however, have shown that there is significant evolution

Table 1
Stacking Results for the CO and [C I] Lines

Transition	ν_0 (GHz)	$z_{\rm min}$	Band	N	$S_\nu\Delta v$ (mJy km s^{-1})	$S_\nu\Delta v$ (mJy km s^{-1})	L' (K km s^{-1} pc^2)
(1)	(2)	(3)	(4)	(5)	(6)	(7)	(8)
Systemic redshift sample (Figure 6)							
CO $J=4\rightarrow3$	461.04	3.0115	3	23	-3.2 ± 4.2	<12.7	$<4.0\times10^8$
[C I] $^3P_1\rightarrow{}^3P_0$	492.16	3.2823	3	16	4.9 ± 6.8	<20.5	$<5.6\times10^8$
CO $J=9\rightarrow8$	1036.91	2.8122	6	23	33.3 ± 12.7	<38.1	$<2.3\times10^8$
CO $J=10\rightarrow9$	1151.99	3.2352	6	16	7.4 ± 16.6	<49.8	$<2.5\times10^8$
Lyα-selected galaxies only							
CO $J=4\rightarrow3$	461.04	3.0115	3	18	-7.3 ± 5.0	<15.0	$<4.7\times10^8$
[C I] $^3P_1\rightarrow{}^3P_0$	492.16	3.2823	3	12	11.0 ± 7.9	<23.8	$<6.5\times10^8$
CO $J=9\rightarrow8$	1036.91	2.8122	6	19	39.5 ± 14.0	<42.2	$<2.6\times10^8$
CO $J=10\rightarrow9$	1151.99	3.2352	6	13	16.2 ± 18.8	<56.5	$<2.8\times10^8$

Note. $\langle z\rangle=3.45$, $\Delta v=300$ km s^{-1}. (1) Stacked transition. (2) Rest frequency. (3) Minimum redshift at which the transition is covered by ASPECS. (4) Band that contains transition. (5) Number of objects in the stack. (6) Line flux in the stack. (7) 3σ upper limit on line flux. (8) 3σ upper limit on line luminosity.

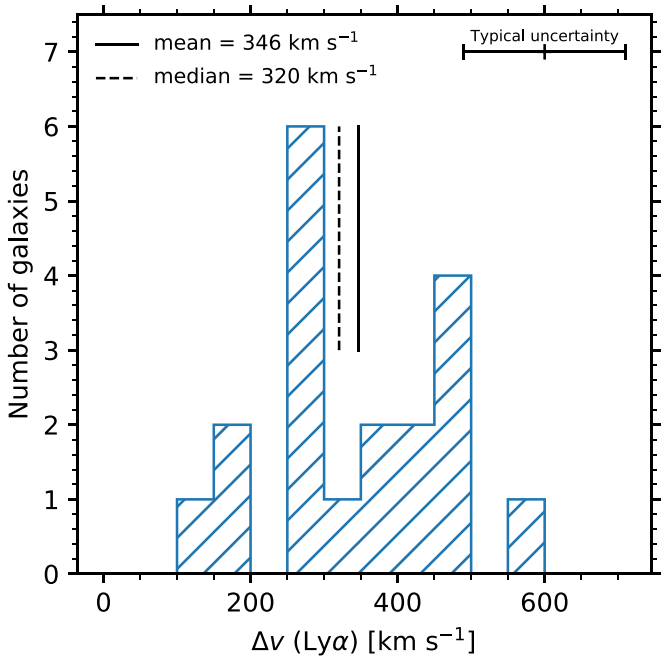

Figure 5. Histogram of the velocity offset of Lyα λ1216 with respect to the systemic redshift, Δv(Lyα). The vertical lines indicate the mean and median velocity offset in the sample. The typical $\pm1\sigma$ uncertainty on the velocity offset is indicated in the top right.

in the CO excitation of gas-mass-selected samples, with the average r_{41} increasing from 0.3 up to 0.6 between $z=1$–2 and $z=2$–3. Indeed, Dessauges-Zavadsky et al. (2017) find $r_{41}=0.60\pm0.17$ in the strongly lensed MACS J0032-arc at $z=3.6$, with a similar $M_*\approx10^{9.7}\,M_\odot$ as our sample average (though significantly higher SFR ≈50 $M_\odot$ yr^{-1}). If the excitation scales with SFR surface density (Daddi et al. 2015; Valentino et al. 2020; Boogaard et al. 2020), this may suggest the excitation to be lower in our galaxies on average. We therefore loosely assume that $r_{41}=0.5\pm0.2$, broadly encompassing the literature values. Note that higher excitation implies a smaller gas mass (Equation (2)). As we are dealing with an upper limit on the gas mass in the first place, we effectively assume a lower limit on the excitation of $r_{41}\geqslant0.3$, in good agreement with observations.

A major uncertainty in the molecular gas estimate comes from $\alpha_{\rm CO}$. For star-forming galaxies at high redshift, "Galactic" conversion factors are typically assumed, consistent with observations in massive star-forming galaxies (Daddi et al. 2010a). However, the value of $\alpha_{\rm CO}$ has been observed to increase strongly at low metallicity (Z; Maloney & Black 1988; Israel 1997), where the decreased shielding leads to dissociation of CO deeper into the clouds (e.g., Wolfire et al. 2010; see Bolatto et al. 2013 for a review). Several calibrations for the metallicity dependence of the CO-to-H_2 conversion factor exist in the literature, both determined empirically (e.g., Leroy et al. 2011; Genzel et al. 2012; Magdis et al. 2012; Schruba et al. 2012; Sandstrom et al. 2013) as well as theoretically (e.g., Wolfire et al. 2010, see also Bolatto et al. 2013).

We adopt the relation from Genzel et al. (2015, also adopted by Tacconi et al. 2018; Dessauges-Zavadsky et al. 2020)

$$\alpha_{\rm CO}(Z)=\alpha_{\rm CO}^{\rm MW}\times\sqrt{10^{-1.27(12+\log({\rm O/H})-8.67)}} \quad (3)$$

$$\times\sqrt{0.67\exp\left(0.36\times10^{-(12+\log({\rm O/H})-8.67)}\right)}, \quad (4)$$

which is the geometrical mean of the curves from Genzel et al. (2012, which follows a power law, as the other literature relations do) and Bolatto et al. (2013, which has a steeper, exponential increase toward very low metallicities). Here, $12+\log({\rm O/H})$ is the gas-phase oxygen abundance, measured on the Pettini & Pagel (2004) scale (for conversion between metallicity scales, see Kewley & Ellison 2008), calibrated to a solar abundance of $12+\log({\rm O/H})_\odot=8.67$ (Asplund et al. 2009) and $\alpha_{\rm CO}^{\rm MW}=4.36\,M_\odot({\rm K\,km\,s^{-1}\,pc^2})^{-1}$, which includes a factor of 1.36 for helium (Strong & Mattox 1996).

To obtain metallicities in the absence of a direct tracer, the mass–metallicity relation can be used (see Section 4.2 for discussion). Genzel et al. (2015) determined the following

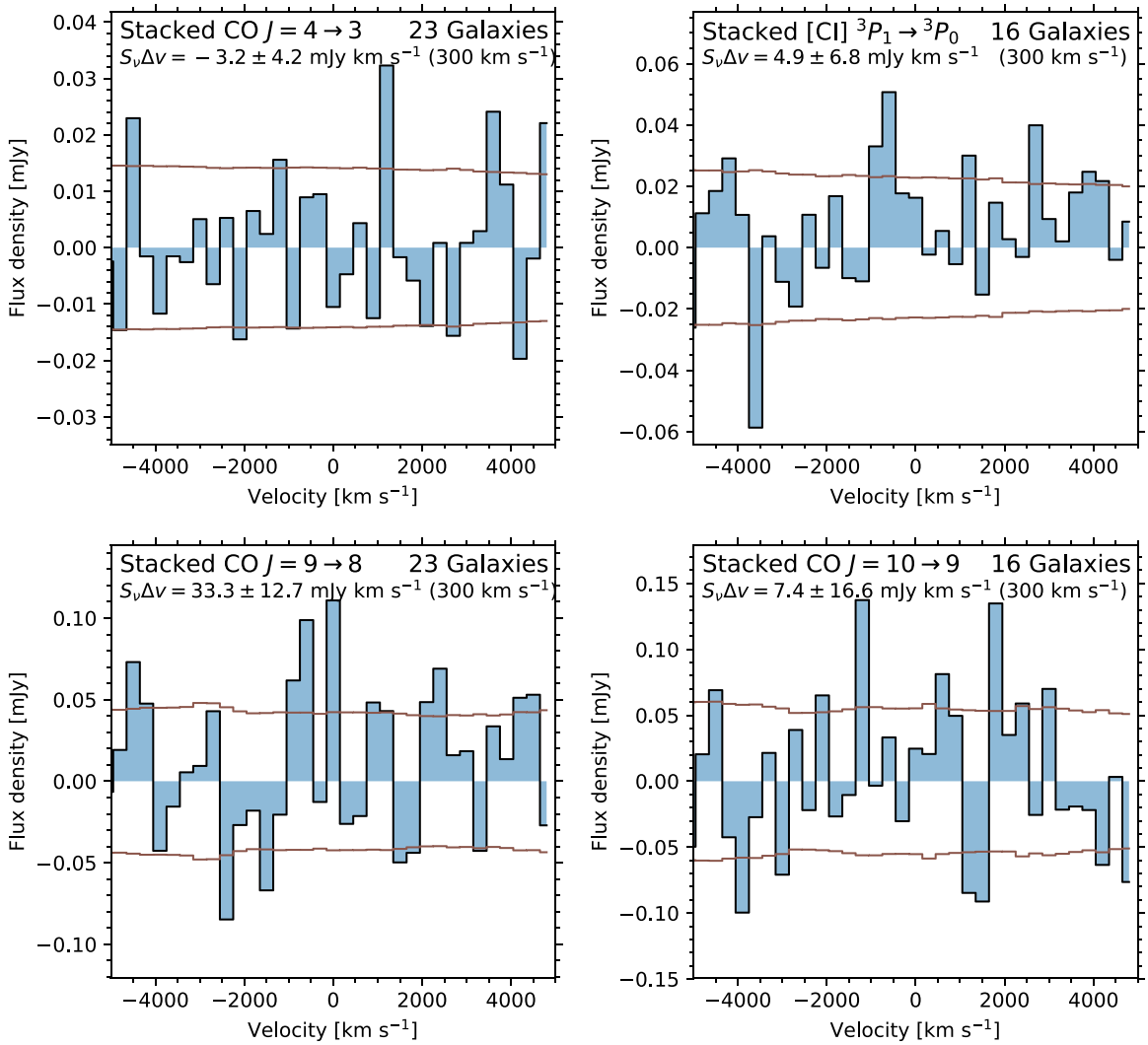

Figure 6. Stacked spectra of the ^{12}CO and [C I] transitions of the full sample. The spectrum is shown in blue and the brown line shows the rms noise (propagated through the $1/\sigma^2$ weighting of the stack). The stacked transition, the number of galaxies in the stack, the integrated line flux in the zero-velocity channel, and the channel width (300 km s^{-1}) are indicated in each panel. We do not detect any emission in any of the transitions and provide 3σ upper limits in Table 1.

mass–metallicity relation:

$$12 + \log(\mathrm{O/H})_{\mathrm{PP04}} = a - 0.087(\log M_* - b(z))^2\,, \quad (5)$$

where $a = 8.74(0.06)$ and $b(z) = 10.4(0.05) + 4.46(0.3)\log(1+z) - 1.78(0.4)\log^2(1+z)$ (uncertainties in brackets), which is determined by combining several relations at different redshifts (Erb et al. 2006; Maiolino et al. 2008; Zahid et al. 2014; Wuyts et al. 2014). Notably, this relation approaches that of Maiolino et al. (2008) determined at $z = 3.5$.

Alternatively, we can determine M_{mol} from [C I], under the assumption of an excitation temperature T_{ex} and a neutral atomic carbon abundance (Weißet al. 2005; see Boogaard et al. 2020 for a detailed description). We adopt $T_{\mathrm{ex}} = 30$ K (Walter et al. 2011; note that the atomic carbon mass is not a strong function of excitation temperature above $T_{\mathrm{ex}} = 20$ K) and an abundance of $[\mathrm{C\,I}]/[\mathrm{H_2}] = 2 \times 10^{-5}$ (Valentino et al. 2018; Boogaard et al. 2020). We will revisit the latter assumption in Section 4.2.

The dust can be used as a third tracer of the molecular gas mass. We compute the dust mass by relying on assumption that the Rayleigh–Jeans (RJ) tail of the dust blackbody at long wavelengths is nearly always optically thin (Scoville et al. 2016). Specifically, we follow Magnelli et al. (2020) and assume a dust opacity of $\kappa_{\nu_0} = 0.0431$ m^2 kg^{-1} at $\nu_0 = 352.6$ GHz (i.e., 850 μm; Li & Draine 2001),[23] a mass-weighted mean dust temperature of $\langle T_{\mathrm{dust}}\rangle_{\mathrm{M}} = 25$ K, and a dust emissivity spectral index of $\beta = 1.8$. As argued by Scoville et al. (2016), the cold dust is the dominant contributor to the dust mass and the RJ tail of the dust emission, and recent studies by Planck and Herschel have found the temperature to be in the range of 15–35 K (e.g., Planck Collaboration et al. 2011; Magnelli et al. 2014). Varying beta between 1.5 and 2.0 (the range typically assumed for the larger grains that dominate the far-infrared emission; e.g., Da Cunha et al. 2008) impacts the dust masses by 20%–40%. Varying the dust temperature between 15 and 35 K has a more significant impact on the inferred gas masses, ranging from a factor of 5.0–0.5, because the observations at rest-frame 275 μm start probing the emission away from the RJ tail and closer to the peak (this is further discussed in Section 4.2). We

[23] As pointed out by Magnelli et al. (2020), assuming a typical gas-to-dust mass ratio of 100 (at solar metallicity), this dust mass absorption cross section is within a few percent of the "ISM" mass absorption cross section calibrated by Scoville et al. (2016, i.e., their $\alpha_{850\ \mu\mathrm{m}}$).

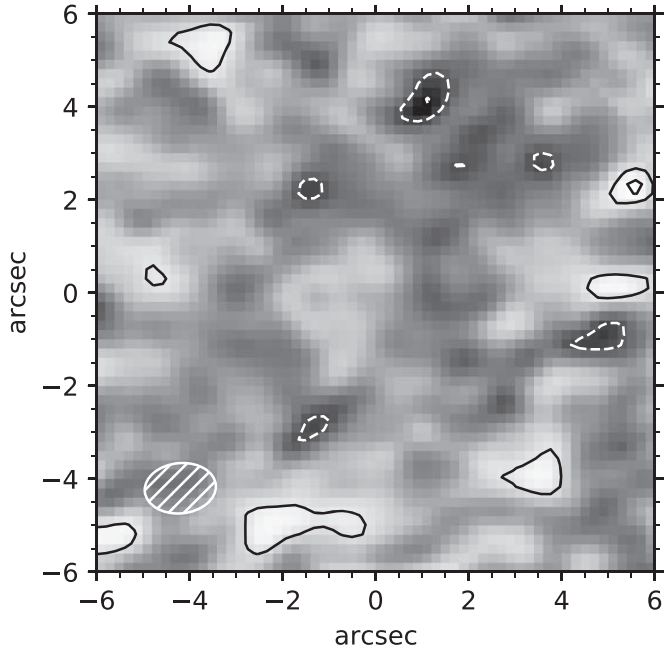

Figure 7. Stack of the 1.2 mm dust continuum. The cutout size is $12'' \times 12''$, and the synthesized beam is indicated in the bottom-left corner. Contours are drawn starting at $\pm 2\sigma$ in steps of $\pm 1\sigma$ (dashed contours indicate a negative signal). No emission is detected at the 3σ level, implying an upper limit of 9 μJy.

correct for the impact of the cosmic microwave background on the equilibrium dust temperature and observed flux density (da Cunha et al. 2013), which increases the inferred mass by 10%.

To convert the dust masses to gas masses, we assume a metallicity-dependent gas-to-dust ratio ($\delta_{\rm GDR} \simeq M_{\rm mol}/M_{\rm dust}$), with $\delta_{\rm GDR}(Z_\odot) = 100$ (Draine et al. 2007), making the common assumption that the gas in our galaxies at $z = 3.45$ is predominantly molecular (e.g., Daddi et al. 2010b; Genzel et al. 2015; Tacconi et al. 2018). The $\delta_{\rm GDR} \propto Z^{\gamma}$ has been observed to decrease close to linearly toward subsolar metallicities (with $\gamma \approx -1$; e.g., Leroy et al. 2011; Magdis et al. 2012; Saintonge et al. 2013; Sandstrom et al. 2013). However, there is increasing evidence of a steeper relation for metallicities below 12+ log(O/H) $\approx$ 8.0–8.1; Rémy-Ruyer et al. (2014) find $\gamma \approx -3.1$ in local galaxies, while observations at $z \sim 2$ suggest that $\gamma < -2.2$ (Coogan et al. 2019), in agreement with the fiducial model from Popping et al. (2017). We explore both regimes, assuming the power-law $\delta_{\rm GDR}(Z)$ relation from Tacconi et al. (2018) for a shallower increase with metallicity. For a steeper $\delta_{\rm GDR}(Z)$ at low metallicity, we adopt the broken power-law relation from Rémy-Ruyer et al. (2014, the $X_{\rm CO,Z}$ case), which we scale to the same assumptions ($12 + \log({\rm O/H})_\odot = 8.67$; $\delta_{\rm GDR}(Z_\odot) = 100$):

$$\delta_{\rm GDR}(Z) = \begin{cases} 10^{2+\gamma_{\rm H}(x-8.67)} & {\rm for} x > 8.1 \\ 10^{0.8+\gamma_{\rm L}(x-8.67)} & {\rm for} x \leqslant 8.1, \end{cases} \quad (6)$$

with $x = 12 + \log({\rm O/H})$. Here $\gamma_{\rm H} = -1$ and $\gamma_{\rm L} = -3.1$ are the power-law slopes at high and low metallicity, respectively. The relation from Tacconi et al. (2018) is obtained from Equation (6) by taking the $x > 8.1$ solution at all metallicities, with $\gamma_{\rm H} = -0.85$.

4.2. Low Metallicity Driving a High Molecular Gas Mass-to-light Ratio

We show the constraints on the molecular gas mass in the context of the molecular gas-to-stellar mass ratio ($\mu_{\rm gas} = M_{\rm mol}/M_*$) and the gas fraction ($f_{\rm gas} = M_{\rm mol}/(M_{\rm mol} + M_*)$), including a literature sample of CO observations at low and high redshifts, in Figure 8. On the basis of the literature sample, we take the mass-selected sample of Sloan Digital Sky Survey galaxies at $z = 0$ from xCOLDGASS (Saintonge et al. 2017), together with the massive, main-sequence-selected galaxies at $z = 0.5$–2.5 from the Plateau de Bure HIgh-z Blue Sequence Survey (PHIBSS1+2) from the Tacconi et al. (2018) compilation and the galaxies from ASPECS at $z = 1.0$–3.6 (Aravena et al. 2019; Boogaard et al. 2019). We supplement these with studies that contain observations of CO in (strongly lensed) star-forming galaxies at $z \geqslant 3$ from Magdis et al. (2012, 2017, using the updated values from Tan et al. 2013), Dessauges-Zavadsky et al. (2015, 2017, which include two sources from Riechers et al. 2010), Gowardhan et al. (2019), and Cassata et al. (2015, based on the sources from Schinnerer et al. 2016). We convert the literature observations to the metallicity-dependent $\alpha_{\rm CO}$ (Equation (4); using the mass–metallicity relation when needed, Equation (5)) and adopt $r_{21} = 0.77$ and $r_{31} = 0.55$ (± 0.1; to remain consistent with Tacconi et al. 2018), though we keep the excitation corrections as assumed by the authors in case these are better constrained through additional line measurements (Boogaard et al. 2020; Cassata et al. 2020).[24]

Assuming conversion factors that apply at solar metallicity ($\alpha_{\rm CO}^{\rm MW} = 4.36$, $\delta_{\rm GDR} = 100$), the stacking results imply gas fractions that appear to be in tension with the observed gas fractions in galaxies at $z \geqslant 3$ at a similar stellar mass (see Figure 8). This is in particular true for stringent limit based on the dust, which places our low-mass galaxies among the lowest gas fractions observed at $z = 3$–4, with $f_{\rm gas} \leqslant 0.5$. For CO, the tension becomes clearer once we take into account that our galaxies are over an order of magnitude lower in stellar mass than the typical galaxy studied in molecular gas at high redshift. The gas fraction in star-forming galaxies is observed to increase toward lower masses and expected to be substantial for low-mass galaxies at these epochs (Scoville et al. 2017; Tacconi et al. 2018; Liu et al. 2019). For reference, we show the predicted gas fraction for a main-sequence galaxy with $M_* = 10^{9.1} \pm 10^{0.2}\ M_\odot$ from Tacconi et al. (2018),[25] taking into account an extra 0.2 dex uncertainty in the average stellar mass, as well as for $M_* = 10^{10}\ M_\odot$ (that is, more massive than the most massive galaxy in our sample). We also show the predicted gas fractions from Liu et al. (2019), based on dust-continuum measurements only, which are higher than those from Tacconi et al. (2018; the relations from Scoville et al. 2017 predict even higher gas fractions). Taking into account the evolution of the gas fraction in low-mass galaxies, the

[24] For example, in the case of ASPECS, the measured $\langle r_{31} \rangle = 0.8$ (Boogaard et al. 2020; Riechers et al. 2020) implies a factor of 1.5× higher gas masses than the average value from Tacconi et al. (2018). Note however that, as argued in Section 4.1, differences in the excitation do not affect the upper limit on the gas mass of our star-forming galaxies at $\langle z \rangle = 3.45$, unless the excitation is significantly lower than our (conservative) lower limit.

[25] We adopt the "$\beta = 0$" scaling relation from Tacconi et al. (2018), assuming a main sequence as observed by Whitaker et al. (2014). Using their alternative "$\beta = 2$" relation instead (which predicts a stronger increase in the gas fractions at lower redshift, with a turnover toward decreasing gas fractions above $z \sim 3$), the upper limits are still below the nominal value, but the limit based on CO falls within the scatter.

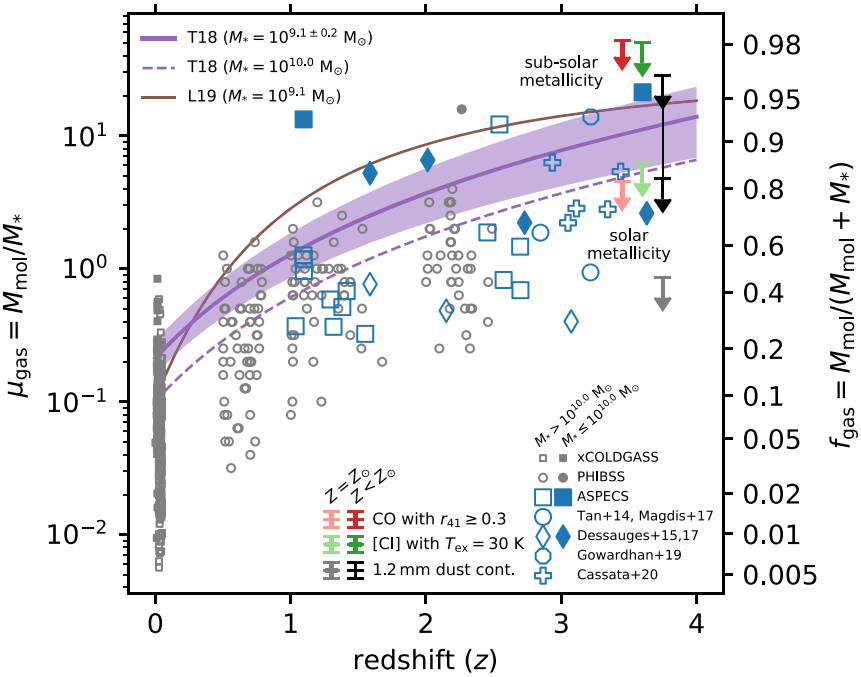

Figure 8. The molecular gas-to-stellar mass ratio (μ_{gas}) and gas fraction (f_{gas}) as a function of redshift. We show a literature sample of star-forming galaxies with CO measurements, focusing on $z \geqslant 3$, separating galaxies with $M_* \leqslant 10^{10}\,M_\odot$ (filled symbols) and $M_* > 10^{10}\,M_\odot$(open symbols). Nearly all galaxies from the literature are significantly more massive than the $\langle z\rangle = 3.45$ star-forming galaxies studied here, which have a median $M_* = 10^{9.1}\,M_\odot$ and SFR $= 10\,M_\odot\,\mathrm{yr}^{-1}$. The upper limit on the gas fraction from CO is shown in red, with the limits at low and high gas fractions corresponding to solar metallicity ($\alpha_{CO}^{MW} = 4.36$; light red) and subsolar metallicity ($\alpha_{CO} = 50$; dark red), respectively, assuming $r_{41} \geqslant 0.3$. The green limit shows the constraints from [C I], for a typical abundance of 2×10^{-5} and a factor 8 lower in the lighter and darker shading, respectively. The gray and black limits show the constraint from the 1.2 mm dust continuum assuming, in order of increasing gas fraction, $\delta_{GDR} = 100$, 550, and 3300, corresponding to solar metallicity and subsolar metallicity with different assumptions for the scaling of $\delta_{GDR} \propto Z'^{\gamma}$. We add horizontal offsets to the upper limits from different tracers for clarity. For comparison, we also show the predictions from Tacconi et al. (2018, based on CO and dust-continuum measurements) for main-sequence galaxies with stellar masses $M_* = 10^{9.1} \pm 10^{0.2}\,M_\odot$ (solid line with shading; 0.2 dex around the median mass of our sample, where shading also includes the uncertainties in the fit of the scaling relation) and $10^{10.0}\,M_\odot$ (dashed; above the most massive galaxy in our sample), and from Liu et al. (2019, based on dust continuum only) for $M_* = 10^{9.1}\,M_\odot$ (solid brown line). Under the assumption of solar metallicity conversion factors, the constraints are in tension with the scaling relations for galaxies in our mass range, while for subsolar metallicity conversion factors, the upper limits are in comfortable agreement.

upper limit based on the CO is also in tension with the expected gas fraction.

At face value, this result suggests that the galaxies in our sample have unexpectedly low molecular gas fractions. However, a more likely explanation is that the assumption of a Galactic α_{CO} and gas-to-dust ratio does not hold for these systems. Indeed, significantly higher conversion factors would be naturally explained by subsolar metallicities for these systems.

In Figure 9, we show the mass–metallicity (MZ) relation from Equation (5) at the average redshift of our sample. We find that the metallicity at the median mass (16th, 84th percentile) of the sample is $12 + \log(\mathrm{O/H}) = 7.7^{+0.3}_{-0.2}$. However, the MZ relation is only an approximate tracer of the metallicity. More directly, the [O III] λ5008/Hβ λ4863 ratio can be used to trace the metallicity, albeit with significant scatter, as the ratio monotonically increases with decreasing metallicity, up to a turnover at $12 + \log(\mathrm{O/H}) \sim 8.0$ (e.g., Curti et al. 2017; Sanders et al. 2020). Because of this turnover, there are two metallicity solutions at a fixed ratio: one on the upper branch (high metallicity) and one on the lower branch (low metallicity). We robustly detect Hβ in two objects, finding high ratios of $\log([\mathrm{O\,III}]/\mathrm{H}\beta) \approx 0.8$ for two (MUSE-1019 and MUSE-6878). This roughly implies a metallicity at the turnover, $12 + \log(\mathrm{O/H}) \sim 8.0$, via the direct method (Curti et al. 2017).[26] We also tentatively detect Hβ λ4863 in a third object (MUSE-6895), yielding a lower ratio (0.35), which implies a high metallicity if it is on the upper branch of the metallicity calibration, in tension with its stellar mass. However, assuming that it follows the (extrapolated) lower branch, this would imply a much lower metallicity of $12 + \log(\mathrm{O/H}) \sim 7.35$ (and an extremely high $\alpha_{CO} \gg 100$), in better agreement with the stellar mass. For the remaining galaxies, we only find (weak) upper limits on the metallicity (conservatively assuming all are on the higher branch).

To obtain an estimate of the average metallicity in the sample, we stack the KMOS spectra using weighted mean and median stacking. Because of the uncertainties in the background level (see Section 2.2.2), we do not normalize the spectra but stack the continuum-subtracted spectra instead, which may introduce a bias toward the brighter objects that go into the stack. Note that, due to the shifting to a common redshift, the skyline residuals are spread throughout the stack, though this problem should be mitigated in the median stack. The stacked spectra are shown in Figure 10. We tentatively detect Hβ λ4863 at 2σ–3σ, measuring $\log([\mathrm{O\,III}]/\mathrm{H}\beta) \approx 0.9 \pm 0.3$, which broadly implies a metallicity of $12 + \log(\mathrm{O/H}) \approx 7.6$–8.0. We do caution against overinterpreting the stack, given the uncertainties mentioned above. It should also be stressed that the mass–metallicity relation only holds on average. For example, Dessauges-Zavadsky et al. (2017) found that the lensed arc at $z = 3.6$ has a higher inferred metallicity from its measured [O III]/Hβ-ratio than predicted from the MZ. While the sample selection could in principle bias the average metallicity, this is not immediately

[26] http://www.arcetri.astro.it/metallicity/calibrazioni.pl

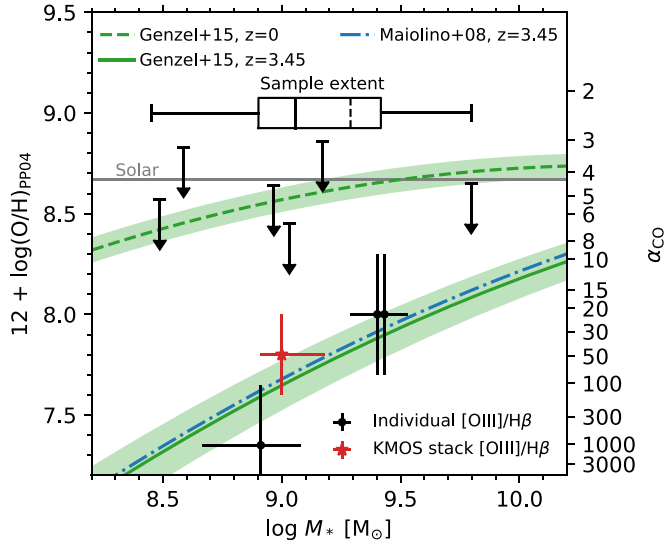

Figure 9. Plot of the mass–metallicity (MZ) relation and the corresponding $\alpha_{CO}(Z)$ (Equations (4) and (5); Genzel et al. 2015), as a function of stellar mass (M_*). The constraints on the MZ relation at $z = 3.45$ come from Maiolino et al. (2008). Metallicity is plotted as $12 + \log(O/H)$ on the Pettini & Pagel (2004) scale. The inset shows a box plot with the whiskers indicating the full stellar mass extent of the sample, the box the interquartile range, the solid line the median, and the dashed line the (linear) mean M_* of the sample. The black points show direct constraints (3σ limits) on the metallicity of a few galaxies via [O III] λ5008/Hβ λ4863, with 0.3 dex uncertainty, using the direct method (Curti et al. 2017), conservatively assuming the upper branch solution for the upper limits. The red star shows the average metallicity from the stack of the KMOS spectra (Figure 10) at the mean stellar mass (error bars correspond to the 16th and 84th percentile). Overall, the measurements are consistent with the MZ relation at the typical redshift of the sample.

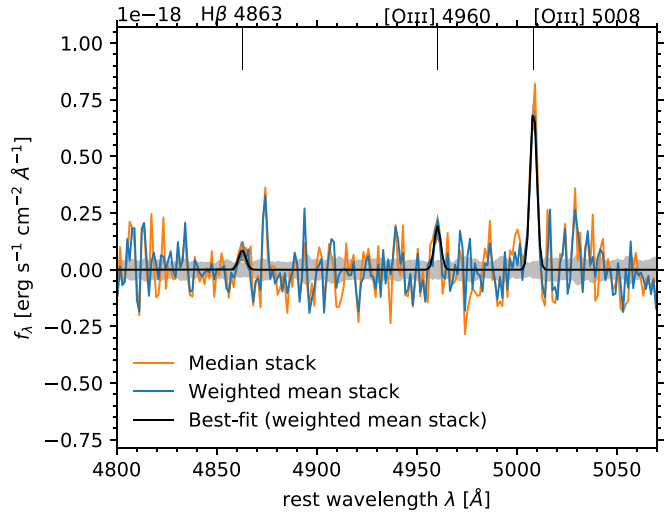

Figure 10. Stacked NIR spectra of the galaxies observed with KMOS (continuum subtracted). We show the median stack (orange), the weighted mean stack (blue, with propagated errors in gray), and the best fit to the weighted mean stack (in black, with uncertainties). We tentatively detect Hβ λ4863, measuring $\log([O\,III]/H\beta) \approx 0.9 \pm 0.3$, which broadly implies a metallicity of $12 + \log(O/H) \approx 7.6$–8.0 (Curti et al. 2017).

obvious, as the selection toward galaxies with a low EW(Lyα) but a high EW([O III]) biases the metallicity in opposite directions and may to some extent cancel out. Overall, the metallicities of the individual galaxies and the average metallicity from the stack are in reasonable agreement with the predictions from the MZ relation (Figure 9), pointing to an average metallicity of $12 + \log(O/H) \approx 7.8 \pm 0.2$ for the galaxies in our sample.

The average metallicity of our sample implies a significantly higher value of $\alpha_{CO} \approx 50$, which places our upper limit in comfortable agreement with the predicted gas fractions (see Figure 8). Notice that the strong, nonlinear increase in the conversion factor with metallicity (Equation (4)) makes the exact value uncertain, particularly in the low-mass range. Furthermore, we caution that there is still debate about the exact relation between α_{CO} and metallicity at low metallicity, mostly due to the difficulty of constraining α_{CO} at low metallicity. In any case, a minimum value of $\alpha_{CO} \geqslant 10$ is required to place the 3σ upper limit on the Tacconi et al. (2018) relation, more than 2 times the Galactic value.

The shallower relations between the gas-to-dust ratio and metallicity yield gas-to-dust ratios that are insufficient to reconcile the observed limit with the scaling relations, which requires a $\delta_{GDR} \geqslant 1200$. For example, we find $\delta_{GDR} \approx 550$ based on Tacconi et al. (2018, see Equation (6)). This points toward a steeper relation between the δ_{GDR} and metallicity in the low-metallicity regime, as suggested by, for example, Rémy-Ruyer et al. (2014) and Coogan et al. (2019) (see Section 4.1). Adopting the relation from Rémy-Ruyer et al. (2014, Equation (6)) yields a significantly higher $\delta_{GDR} \approx 3300$, again placing our upper limit in comfortable agreement with the expected gas fraction. Alternatively, a dust temperature of $T_{dust} < 20$ K (as opposed to 25 K) can also reconcile the difference with a lower δ_{GDR}. However, given the stronger radiation field expected at low metallicity, it is not clear that the dust temperatures would be much lower than assumed.

Independent of CO and the dust, we reach similar conclusions using [C I] instead. While a typical abundance ratio of 2×10^{-5} predicts a gas mass that is marginally consistent with the scaling relations, assuming a lower abundance (e.g., 8×; loosely based on the metallicity) easily yields a limit that is fully consistent with the scaling relations, with a $\approx 2\times$ lower abundance being minimally required (see Figure 8). Note that the metallicity impacts CO and [C I] in different ways, however, such that [C I] may be a preferred over CO as a tracer of cold gas in low-metallicity environments (we will come back to this point in Section 4.4).

For reference, we collect the different molecular gas masses and gas-to-stellar mass ratios that are discussed in this section, and shown in Figure 8, in Table 2.

4.3. Contribution to the Cosmic Molecular Gas Density

The galaxies under study are below the detection threshold of current $\rho_{mol}(z)$ surveys (e.g., Decarli et al. 2020; Riechers et al. 2019; Decarli et al. 2019). Still, their potentially high gas mass-to-light ratios imply that they could have a significant contribution to the total cosmic molecular gas density. Assuming the average gas masses derived from the stacks are representative of all 67 galaxies in the photometric catalog down to $H_{F160W} = 26$ (cf. Figure 1), we compute the total contribution of these galaxies to the cosmic molecular gas density, $\rho(3.0115 < z < 3.812)$. We adopt the solar, the minimum, and the subsolar conversion factors from Section 4.2, and $r_{41} = 0.5$, and shift the CO-based determinations of ρ_{mol} at $z > 0$ to match our assumption on α_{CO}^{MW}. The result can be seen in Figure 11. Because the upper limits are not stringent enough, the results are inconclusive. On one hand, they do not exclude the possibility that a significant amount of molecular gas is missed due to the

Table 2
Upper Limits (3σ) on the Molecular Gas Mass and Molecular Gas-to-stellar Mass Ratio under Different Assumptions

Tracer	Conversion factor	$\langle M_{\rm mol}\rangle$ ($\times 10^9\ M_\odot$)	$\langle \mu_{\rm gas}\rangle$
(1)	(2)	(3)	(4)
Solar metallicity			
CO $J=4\rightarrow3$	$\alpha_{\rm CO}=4.36$	<5.74	<4.56
[C I] $^3P_1\rightarrow{}^3P_0$	$X_{\rm [C\ I]}=2\times10^{-5}$	<7.91	<6.29
S_ν(1.2 mm)	$\delta_{\rm GDR}=100$	<1.09	<0.87
Subsolar metallicity			
CO $J=4\rightarrow3$	$\alpha_{\rm CO}=50$	<65.9	<52.3
[C I] $^3P_1\rightarrow{}^3P_0$	$X_{\rm [C\ I]}=2.5\times10^{-6}$	<63.3	<50.3
S_ν(1.2 mm)	$\delta_{\rm GDR}=550$	<5.99	<4.76
S_ν(1.2 mm)	$\delta_{\rm GDR}=3300$	<36.0	<28.6

Note. Derived from the upper limits (see Section 3.2 and Table 1) for the full systemic redshift sample ($\langle M_*\rangle = 10^{9.1}\ M_\odot$) as explained in Section 4.1, with metallicity-dependent conversion factors as listed. (1) Molecular gas tracer. (2) Adopted (metallicity dependent) conversion factor ($X_{\rm [C\ I]}\equiv$ [C I]/[H_2]). (3) Upper limit on molecular gas mass. (4) Upper limit on $\langle\mu_{\rm gas}\rangle = \langle M_{\rm mol}\rangle/\langle M_*\rangle$.

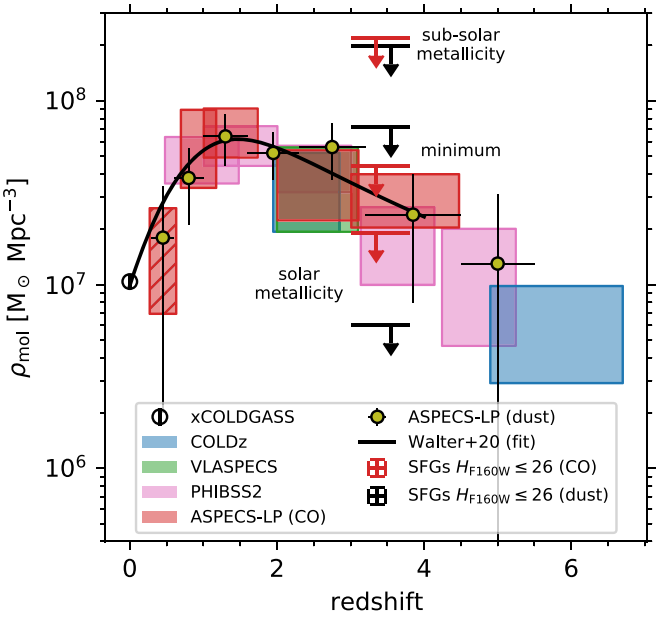

Figure 11. Cosmic molecular gas density as a function of redshift. The literature data are from Fletcher et al. (2021; xCOLDGASS), Riechers et al. (2019; COLDz), Riechers et al. (2020; VLASPECS), Lenkić et al. (2020; PHIBSS2), Decarli et al. (2020; ASPECS-LP CO), and Magnelli et al. (2020; ASPECS-LP dust), and we also show the best fit from Walter et al. (2020). We show the estimates on the upper limit on the cosmic molecular density for all galaxies with $H_{\rm F160W}\leqslant 26$ at $3.0115 < z < 3.812$, as derived from CO (red; assuming $r_{41}=0.5$) and the dust continuum (black), under the assumption our stacked averages are representative for the larger population. The different limits are for conversion factors ($\alpha_{\rm CO}$, $\delta_{\rm GDR}$) = (4.36, 100), (10, 1200), and (50, 3300), corresponding to solar metallicity, the minimum value based on Section 4.2, and the best-estimate subsolar metallicity (the CO-based literature data are scaled to match our assumption on $\alpha_{\rm CO}^{\rm MW}$). The upper limits do not rule out a large amount of molecular gas in lower mass galaxies (that would have been missed in previous surveys, due to their high gas mass-to-light ratio), but are equally consistent with a smaller contribution to the total molecular gas budget.

high gas mass-to-light ratio of star-forming galaxies at these redshifts. On the other hand, it is equally possible that their contribution is significantly smaller, implying that their molecular gas signal lies well below the detection threshold, even in stacks. We caution that the strong increase in the conversion factor with decreasing metallicity (especially for the lowest metallicity sources) is a significant source of uncertainty when extrapolating the averages to sources over a larger range in mass and metallicity. We therefore also determine upper limits for the more massive galaxies in the sample only (with $M_*\geqslant10^9\ M_\odot$ and $\geqslant10^{9.5}\ M_\odot$, computing their average conversion factors from the mass–metallicity relation). The limits on $\rho_{\rm mol}$ are slightly stronger for these subsamples because, while the stacks are slightly less constraining, the estimated $\alpha_{\rm CO}$ and $\delta_{\rm GDR}$ are lower, as well as the number of sources in the volume. The results fall in between the minimum and subsolar values of the magnitude-limited sample but do not alter the conclusions overall

4.4. Implications for Observing Molecular Gas in Low-metallicity Galaxies at High Redshift

The evolution of the metallicity of star-forming galaxies with redshift has significant implications for the detectability of molecular gas at $z\geqslant3$. Even in the local universe, detecting CO in low-metallicity dwarf galaxies has been challenging (e.g., Schruba et al. 2012; Hunt et al. 2015). The substantial CO-to-H_2 conversion factor and gas-to-dust ratios inferred for our low-mass, low-metallicity galaxies imply that detecting the molecular gas reservoir in these galaxies will be very challenging on an individual basis, even with modern instruments. Similar conclusions are also reached for more massive galaxies at subsolar metallicities (e.g., Tan et al. 2013; Coogan et al. 2019). Tan et al. (2013) have shown that under the assumption of an MZ–$\alpha_{\rm CO}$ relation similar to the one adopted here, the expected CO luminosity for a star-forming galaxy on the main sequence rapidly declines, due to the metallicity evolution. This raises the interesting question of how the molecular gas content can be best constrained in subsolar-metallicity star-forming galaxies at high redshift.

There are significant uncertainties in deriving a total dust and gas mass from the dust continuum in the low-metallicity regime. Variations in the process and balance of dust formation and destruction at low metallicity, as well as differences in grain composition and size distribution can have a major impact on the gas-to-dust ratio, the dust emissivity, and emerging dust spectrum (e.g., Rémy-Ruyer et al. 2014; see also Draine et al. 2007). In addition to these complications, the fainter part of the Rayleigh–Jeans tail at long wavelengths has to be probed, such that the blackbody is dominated by cold dust, which dominates the mass and the uncertainty in the (unknown) mass-weighted dust temperature is minimized (e.g., Scoville et al. 2016).

At low metallicity, CO also becomes an increasingly poor tracer of the total molecular gas reservoir. Because of the lower dust abundance at low metallicity, CO is dissociated and ionized into C and C^+ deeper into the clouds, while the H_2 self-shields against photodissociation (Gnedin & Draine 2014), resulting in an increasing volume of H_2 gas that is not traced by CO at low metallicity (e.g., Wolfire et al. 2010). This provides motivation to investigate and develop the theoretical underpinning for other species as tracers of the molecular gas, such

as the fainter [C I] lines (e.g., Weißet al. 2003, 2005; Papadopoulos et al. 2004; see also Valentino et al. 2018; Boogaard et al. 2020), but in particular also [C II] $\lambda158$ μm.

The bright [C II] $^3P_{3/2} \rightarrow {}^3P_{1/2}$ line at 158 μm is one of the foremost cooling lines of the ISM, also at low metallicity (where it is outranked only by the high-ionization line [O III] $\lambda88$ μm at 35 eV; e.g., Cormier et al. 2015, 2019) and its high luminosity allows it to be observed in star-forming galaxies out to the highest redshifts (Ouchi et al. 2013; Ota et al. 2014; Capak et al. 2015; Maiolino et al. 2015; Knudsen et al. 2016; Pentericci et al. 2016; Bradač et al. 2017; Matthee et al. 2017, 2019; Hashimoto et al. 2018; Smit et al. 2018; Carniani et al. 2018a, 2018b, 2020; Laporte et al. 2019; Bakx et al. 2020; Béthermin et al. 2020; Harikane et al. 2020; Le Fèvre et al. 2020). With an ionization potential of 11.3 eV (that is, lower than H I at 13.6 eV), [C II] can arise in both the neutral and ionized medium, though it becomes an increasingly better tracer of the neutral ISM toward lower metallicities (Croxall et al. 2017; Cormier et al. 2019; see also Díaz-Santos et al. 2017) potentially due to the carbon in the H II regions being further ionized into C^{++} (as witnessed by the shift in the ionization balance to high ionization lines, also see in some high-z sources, e.g., Pavesi et al. 2016; Harikane et al. 2020, see also Carniani et al. 2020). While, as a cooling line, [C II] is in principle sensitive to the heating rate (and not the molecular gas mass), it may be calibrated as a molecular gas tracer (Zanella et al. 2018). As such, [C II] can potentially outperform other tracers of the molecular gas mass, in particular in low-metallicity environments (e.g., Madden et al. 2020). As [C II] is already seeing use as a tracer of the molecular gas at high redshift (e.g., Dessauges-Zavadsky et al. 2020), its use to this end should be further investigated both observationally and theoretically.

5. Summary and Conclusions

We present constraints on the molecular gas signal for a sample of 24 star-forming galaxies at $\langle z \rangle = 3.45$, with a median $M_* = 10^{9.1}\,M_\odot$, in the Hubble Ultra Deep Field (HUDF). Based on their Lyα and $H_{\rm F160W}$ selection (Figure 1), they show relatively low $\mathrm{EW}^0_{\mathrm{Ly}\alpha} \approx 20$ Å ($L_{\mathrm{Ly}\alpha} = 0.2\,L^*_{\mathrm{Ly}\alpha}$) and rest-frame UV spectra similar to star-forming galaxies at the same epoch (see Figure 4). We efficiently follow-up Lyα-selected galaxies from the MUSE HUDF Survey, with near-infrared spectroscopy from KMOS and MOSFIRE to determine their systemic redshifts (Figure 2 and Figure 12) and stack the molecular line emission from the ALMA Spectroscopic Survey in the HUDF (ASPECS). Our main results are as follows:

1. We determine systemic redshifts from the rest-frame UV and rest-frame optical features, finding an average velocity offset of $\langle \Delta v(\mathrm{Ly}\alpha) \rangle = 346$ km s^{-1} (with a 100 to 600 km s^{-1} range) consistent with the relatively low $\mathrm{EW}^0_{\mathrm{Ly}\alpha}$ of the sample (Figure 5).
2. Stacking the signal from ^{12}CO $J = 4 \rightarrow 3$ and [C I] $^3P_1 \rightarrow {}^3P_0$ (as well as the ^{12}CO $J = 9 \rightarrow 8$ and $J = 10 \rightarrow 9$ lines), we do not find any detections and determine 3σ upper limits on the line luminosities of 4.0×10^8 K km s^{-1} pc^2 and 5.6×10^8 K km s^{-1} pc^2, respectively, for a line width of 300 km s^{-1} (see Figure 6 and Table 1; also for the limits on the higher-J lines). Stacking the dust continuum at 1.2 mm and 3 mm, we find 3σ upper limits on the flux densities of $S_\nu \leqslant 9$ μJy and 1.2 μJy, respectively (Figure 7).
3. Comparing the inferred molecular fraction from CO and the dust continuum to scaling relations, we find that assuming a "Galactic" $\alpha_{\mathrm{CO}}^{\mathrm{MW}} = 4.36$ and $\delta_{\mathrm{GDR}} = 100$ significantly underpredicts the expected molecular gas mass (Figure 8). In order to reconcile our measurements with the published scaling relations from Tacconi et al. (2018) would require an $\alpha_{\mathrm{CO}} \geqslant 10$ and $\delta_{\mathrm{GDR}} \geqslant 1200$. This result either implies that our galaxies have unexpectedly low gas fractions or that the assumption of solar-metallicity conversion factors breaks down.
4. Using the mass–metallicity relation, as well as constraints from [O III] $\lambda5008/\mathrm{H}\beta$ $\lambda4863$ (Figure 10), we predict an average metallicity of our sample of $12+\log(\mathrm{O/H}) = 7.8 \pm 0.2$, that is, significantly subsolar. This implies a high $\alpha_{\mathrm{CO}} \approx 50$, making our result consistent with the expected (high) gas fractions at $z = 3.5$ (Figure 9).
5. An approximately linear scaling relation between the gas-to-dust ratio and metallicity ($\delta_{\mathrm{GDR}} \propto \gamma^{-0.85}$; Tacconi et al. 2018) yields $\delta_{\mathrm{GDR}} \approx 550$, which is insufficient to reconcile the limit based on the dust with the scaling relations. Using a steeper relation at low metallicity ($\delta_{\mathrm{GDR}} \propto \gamma^{-3.1}$ at $12 + \log(\mathrm{O/H}) \leqslant 8.1$; Rémy-Ruyer et al. 2014) instead yields $\delta_{\mathrm{GDR}} \approx 3300$, making our upper limit consistent again (Figure 8).
6. Independent of the CO, we find a similar tension from the [C I] luminosity, which implies a [C I]/[H_2] abundance lower than that in massive star-forming galaxies such as the Milky Way (Figure 8).
7. Based on the results, we compute the upper limit on the contribution of all galaxies with $H_{\mathrm{F160W}} \leqslant 26$ to the cosmic molecular gas density $\rho_{\mathrm{mol}}(z = 3.0115-3.812)$. The upper limits are not constraining enough to exclude the possibility of a significant contribution from these galaxies, which lie below the detection threshold of current surveys, to the cosmic molecular gas density.

The results of this work exemplify the difficulty in obtaining molecular gas mass estimates in low-metallicity environments, which are expected to be more prevalent in typical star-forming galaxies at $z \geqslant 3$. Given the uncertainties associated with the dust and CO at low metallicity, we argue for the further observational and theoretical development of alternative tracers of the molecular gas reservoir, such as the bright [C II] $\lambda158$ μm line, that should be more easily observable with ALMA. Obtaining accurate constraints on the gas-phase metallicity of high-redshift galaxies will be key in this regard and one of the key pieces of information that the James Webb Space Telescope will be able to provide.

We would like to thank the referee for a constructive and helpful report. L.A.B. is grateful to Corentin Schreiber for assisting with the near-infrared spectroscopy during the early stages of this work. L.A.B. acknowledges support from the Leids Kerkhoven-Bosscha Fonds under subsidy numbers 18.2.074 and 19.1.147. D.R. acknowledges support from the National Science Foundation under grant numbers AST-1614213 and AST-1910107. D.R. also acknowledges support from the Alexander von Humboldt Foundation through a Humboldt Research Fellowship for Experienced Researchers.

A.F. acknowledges the support from grant PRIN MIUR 201720173ML3WW_001. J.B. acknowledges support by Fundação para a Ciência e a Tecnologia (FCT) through the research grants UID/FIS/04434/2019, UIDB/04434/2020, UIDP/04434/2020. H.I. acknowledges support from JSPS KAKENHI grant No. JP19K23462. This work is based on observations collected at the European Southern Observatory under ESO programs 094.A-2089(B), 095.A-0010(A), 096.A-0045(A), 096.A-0045(B), 099.A-0858(A), and 0101.A-0725 (A). This paper makes use of the following ALMA data: ADS/JAO.ALMA#2016.1.00324.L. ALMA is a partnership of ESO (representing its member states), NSF (USA), and NINS (Japan), together with NRC (Canada), NSC and ASIAA (Taiwan), and KASI (Republic of Korea), in cooperation with the Republic of Chile. The Joint ALMA Observatory is operated by ESO, AUI/NRAO, and NAOJ. The National Radio Astronomy Observatory is a facility of the National Science Foundation operated under cooperative agreement by Associated Universities, Inc. This work was supported by a NASA Keck PI Data Award, administered by the NASA Exoplanet Science Institute. Data presented herein were obtained at the W. M. Keck Observatory from telescope time allocated to the National Aeronautics and Space Administration through the agency's scientific partnership with the California Institute of Technology and the University of California. The Observatory was made possible by the generous financial support of the W. M. Keck Foundation. The authors wish to recognize and acknowledge the very significant cultural role and reverence that the summit of Maunakea has always had within the indigenous Hawaiian community. We are most fortunate to have the opportunity to conduct observations from this mountain.

Facilities: ALMA, VLT:Yepun (MUSE), VLT:Antu (KMOS), Keck I (MOSFIRE).

Software: TOPCAT (Taylor 2005), GNUASTRO (Akhlaghi & Ichikawa 2015), IPYTHON (Perez & Granger 2007), NUMPY (Van Der Walt et al. 2011), MATPLOTLIB (Hunter 2007), ASTROPY (The Astropy Collaboration et al. 2013, 2018), CASA (McMullin et al. 2007).

Appendix A
Spectra

The rest-frame UV (MUSE) and near-IR (KMOS, MOSFIRE) spectra of all galaxies in the sample are shown in Figure 12 (except for the galaxy already shown in Figure 2).

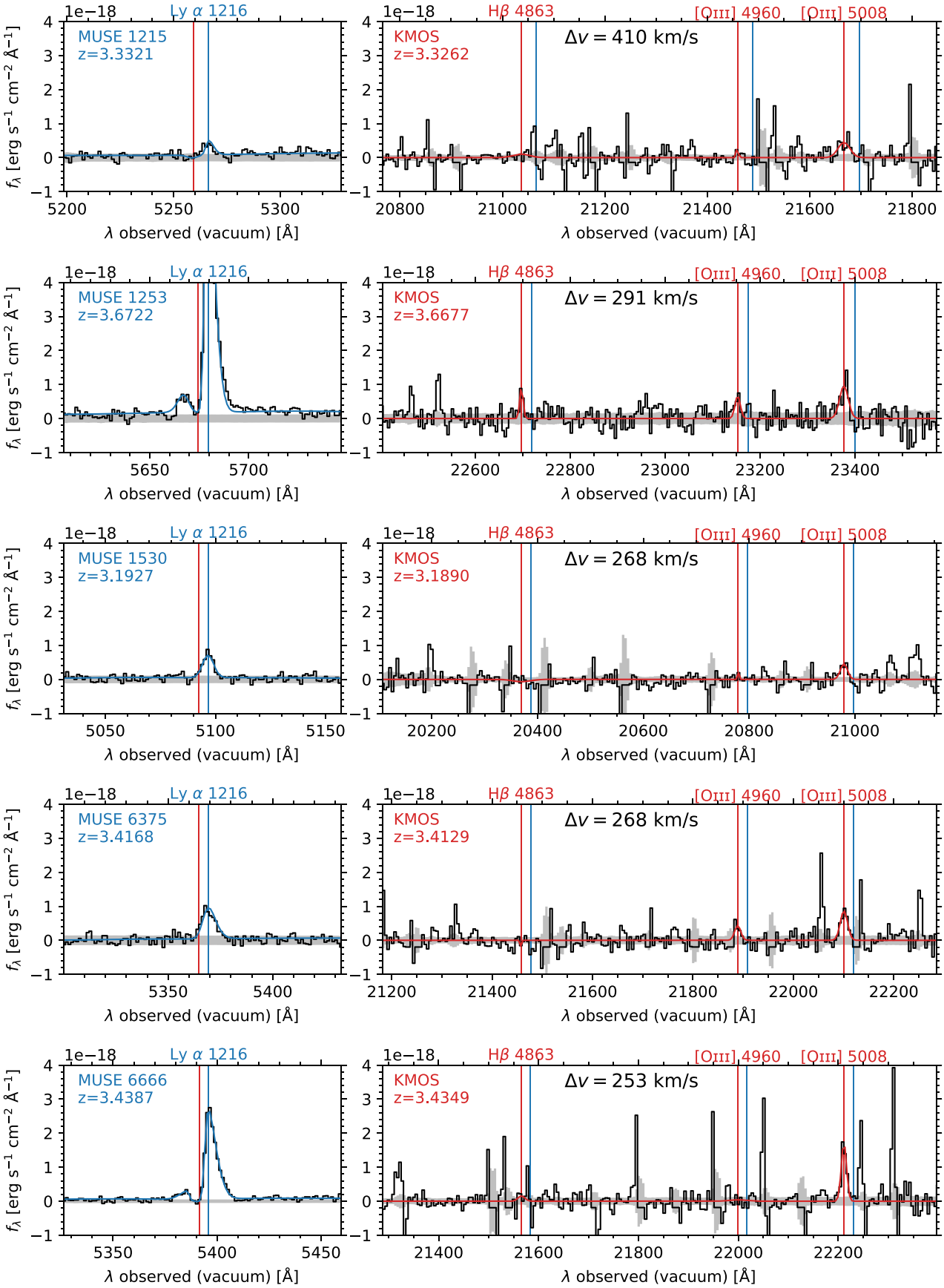

Figure 12. Rest-frame ultraviolet and optical spectra for the galaxies with near-infrared follow-up. The left panel shows the MUSE spectrum surrounding the Lyα line. The right panel shows the continuum-subtracted KMOS or MOSFIRE spectrum (indicated in the figure) around the Hβ and [O III] lines. In both panels the vertical blue and red lines indicate the redshift of Lyα and the systemic redshift, respectively, determined from the fit to the spectrum (shown in the same color). All spectra show a positive velocity offset between the red peak of Lyα and the systemic redshift.

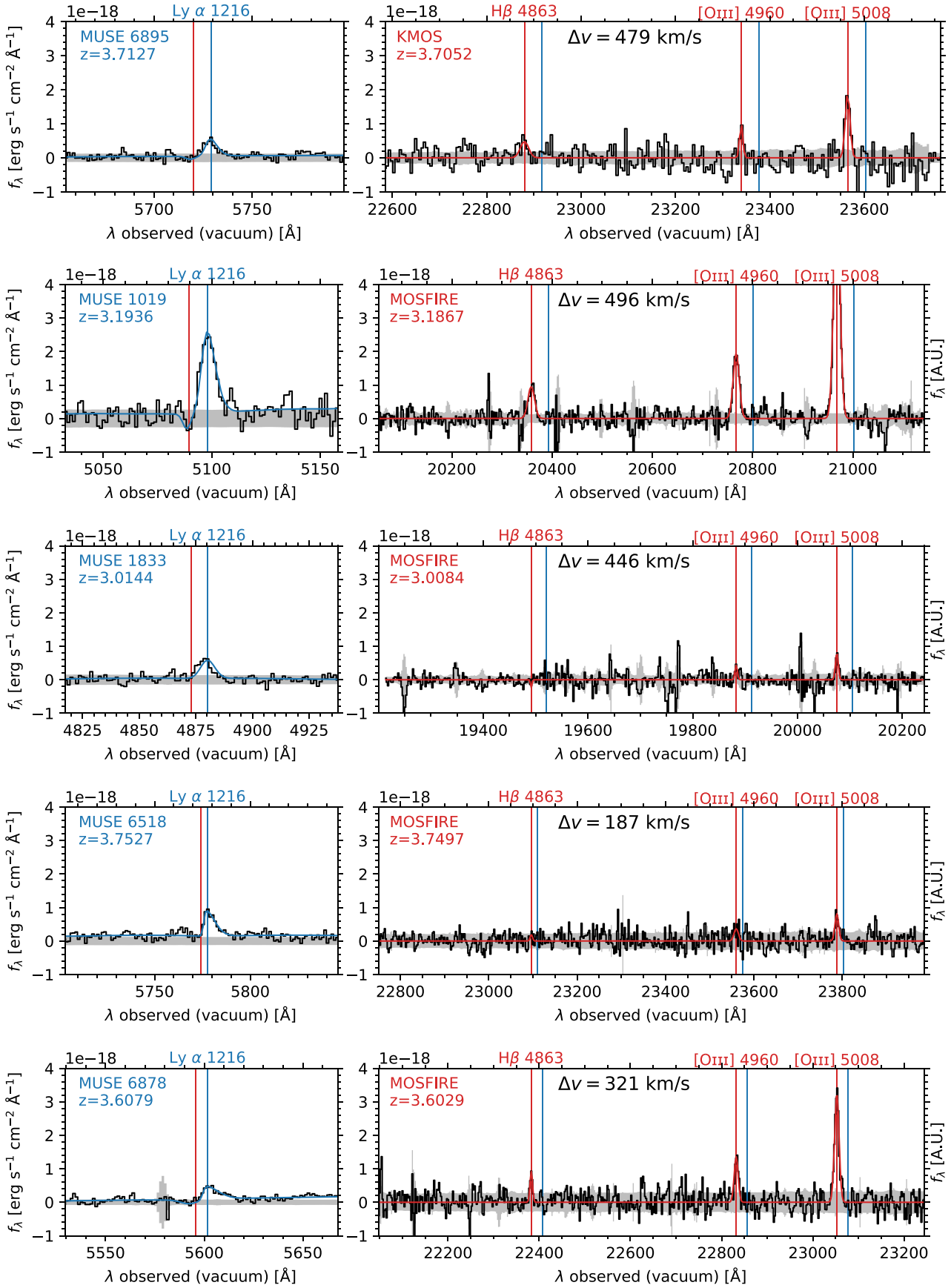

Figure 12. (Continued.)

Appendix B
Table

The coordinates, (systemic) redshifts, and physical properties of the sample of $3.0115 < z < 3.812$ star-forming galaxies are listed in Table 3.

Table 3
Coordinates, (Systemic) Redshifts, and Physical Properties of the Sample of $3.0115 < z < 3.812$ Star-forming Galaxies

ID	RAF ID	α_{J2000}	δ_{J2000}	$z_{\mathrm{Ly}\alpha}^{\mathrm{red}}$	$\delta(z_{\mathrm{Ly}\alpha}^{\mathrm{red}})$ (km s^{-1})	z_{sys}	$\delta(z_{\mathrm{sys}})$ (km s^{-1})	Source	$\Delta v(\mathrm{Ly}\alpha)$ (km s^{-1})	$\log M_*$ ($M_\odot$)	log SFR ($M_\odot$ yr^{-1})
(1)	(2)	(3)	(4)	(5)	(6)	(7)	(8)	(9)	(10)	(11)	(12)
50	9110	53.16284897	−27.77162645	3.33015 ± 0.00086	59.5	3.32349 ± 0.00027	18.7	MUSE EM	461.8 ± 62.5	$9.15^{+0.10}_{-0.12}$	$1.122^{+0.10}_{-0.10}$
82	6627	53.1515512	−27.7853475	3.60777 ± 0.00006	3.9	3.60493 ± 0.00080	52.1	MUSE EM	184.9 ± 52.3	$9.00^{+0.10}_{-0.10}$	$0.792^{+0.10}_{-0.17}$
106	9863	53.16372638	−27.77907551	3.28171 ± 0.00009	6.3	3.27648 ± 0.00012	8.4	MUSE EM	366.6 ± 10.5	$8.45^{+0.10}_{-0.10}$	$0.547^{+0.10}_{-0.10}$
118	23839	53.15708801	−27.78026883	3.02127 ± 0.00056	41.7	3.01727 ± 0.00017	12.7	MUSE EM	298.5 ± 43.7	$8.78^{+0.10}_{-0.20}$	$0.462^{+0.10}_{-0.10}$
1019	8002	53.16492565	−27.76512153	3.19361 ± 0.00088	62.9	3.18669 ± 0.00002	1.4	MOSFIRE	495.5 ± 63.0	$9.43^{+0.10}_{-0.10}$	$1.387^{+0.10}_{-0.10}$
…	…	…	…	…	…	3.18579 ± 0.00026	18.6	MUSE ABS	560.1 ± 65.7	…	…
1059	8203	53.15344247	−27.76611934	3.80588 ± 0.00005	3.1	3.80122 ± 0.00199	124.3	MUSE ABS	291.0 ± 124.4	$9.70^{+0.10}_{-0.10}$	$1.267^{+0.10}_{-0.10}$
1087	3506	53.16790037	−27.7979532	3.46259 ± 0.00019	12.8	3.45675 ± 0.00097	65.2	MUSE ABS	392.8 ± 66.6	$9.55^{+0.10}_{-0.10}$	$1.112^{+0.10}_{-0.10}$
1088	6012	53.15257181	−27.79384452	…	…	3.08224 ± 0.00039	28.6	MUSE ABS	…	$9.65^{+0.10}_{-0.10}$	$1.472^{+0.10}_{-0.10}$
1113	8528	53.16993928	−27.76833978	3.09022 ± 0.00005	3.7	3.08803 ± 0.00281	206.1	KMOS	160.6 ± 206.2	$9.17^{+0.17}_{-0.10}$	$0.917^{+0.10}_{-0.10}$
…	…	…	…	…	…	3.08520 ± 0.00065	47.7	MUSE ABS	368.4 ± 47.9	…	…
1138	8308	53.14850621	−27.77728375	3.61287 ± 0.00266	172.9	3.60520 ± 0.00047	30.6	MUSE ABS	499.3 ± 175.9	$9.40^{+0.11}_{-0.10}$	$1.567^{+0.10}_{-0.10}$
1215	9247	53.1487158	−27.77294489	3.33215 ± 0.00155	107.3	3.32623 ± 0.00104	72.1	KMOS	410.2 ± 129.4	$9.87^{+0.10}_{-0.10}$	$1.092^{+0.17}_{-0.10}$
…	…	…	…	…	…	3.32594 ± 0.00053	36.7	MUSE ABS	430.4 ± 113.5	…	…
1253	8783	53.17824938	−27.77399604	3.67218 ± 0.00096	61.6	3.66765 ± 0.00421	270.4	KMOS	291.0 ± 277.6	$8.59^{+0.10}_{-0.10}$	$0.587^{+0.10}_{-0.10}$
…	…	…	…	…	…	3.66896 ± 0.00067	43.0	MUSE EM	206.8 ± 75.2	…	…
1360	37765	53.17926551	−27.78289487	3.66696 ± 0.00161	103.4	3.66479 ± 0.00284	182.5	MUSE ABS	139.5 ± 209.9	$9.06^{+0.12}_{-0.10}$	$1.027^{+0.10}_{-0.28}$
1530	7002	53.17666134	−27.78380467	3.19270 ± 0.00112	80.1	3.18896 ± 0.00036	25.8	KMOS	267.7 ± 84.2	$8.97^{+0.10}_{-0.10}$	$0.772^{+0.10}_{-0.10}$
1833	3673	53.1524905	−27.79770827	3.01437 ± 0.00178	132.9	3.00842 ± 0.00009	6.7	MOSFIRE	445.0 ± 133.3	$8.49^{+0.14}_{-0.10}$	$0.362^{+0.10}_{-0.36}$
6375	22525	53.14339467	−27.78800227	3.41682 ± 0.00160	108.6	3.41287 ± 0.01914	1300.3	KMOS	268.3 ± 1306.0	$8.79^{+0.10}_{-0.10}$	$0.882^{+0.10}_{-0.10}$
6518[a]	52206	53.14325211	−27.7868279	3.75265 ± 0.00062	39.1	3.74969 ± 0.00020	12.6	MOSFIRE	186.8 ± 41.1	…	…
6666	24954	53.15957552	−27.7767193	3.43869 ± 0.00021	14.2	3.43494 ± 0.00024	16.2	KMOS	253.5 ± 21.6	$9.03^{+0.10}_{-0.10}$	$0.902^{+0.10}_{-0.12}$
…	…	…	…	…	…	3.43492 ± 0.00008	5.4	MUSE EM	254.8 ± 15.2	…	…
6878	7843	53.13953672	−27.78067557	3.60787 ± 0.00090	58.6	3.60020 ± 0.00064	41.7	MUSE ABS	499.8 ± 72.0	$9.40^{+0.10}_{-0.11}$	$1.387^{+0.10}_{-0.13}$
…	…	…	…	…	…	3.60295 ± 0.00006	3.9	MOSFIRE	320.4 ± 58.7	…	…
6883	9832	53.17629722	−27.77891257	3.19503 ± 0.00222	158.6	3.18724 ± 0.00040	28.6	MUSE ABS	557.7 ± 161.5	$9.56^{+0.10}_{-0.10}$	$1.407^{+0.10}_{-0.10}$
6895	5742	53.1759691	−27.79261283	3.71273 ± 0.00194	123.4	3.70409 ± 0.00079	50.3	MUSE ABS	550.6 ± 133.5	$8.41^{+0.10}_{-0.10}$	$0.497^{+0.10}_{-0.10}$
…	…	…	…	…	…	3.70522 ± 0.00020	12.7	KMOS	478.5 ± 124.3	…	…
8041	8635	53.1755829	−27.76874786	…	…	3.69700 ± 0.00172	109.8	MUSE ABS	…	$9.52^{+0.10}_{-0.10}$	$1.317^{+0.10}_{-0.16}$
8091	5468	53.14920592	−27.79147296	…	…	3.55707 ± 0.00116	76.3	MUSE ABS	…	$9.27^{+0.10}_{-0.10}$	$1.242^{+0.10}_{-0.10}$
8103	5741	53.17592521	−27.79246095	…	…	3.70527 ± 0.00027	17.2	MUSE EM	…	$8.60^{+0.10}_{-0.10}$	$0.677^{+0.10}_{-0.16}$

Notes. (1) MUSE ID. (2) Rafelski et al. (2015) ID. (3) R.A., (4) decl. (5) Redshift measured from Lyα λ1216 (the red peak, in the case of a double-peaked line). (6) Velocity uncertainty on redshift. (7) Systemic redshift. (8) Velocity uncertainty on systemic redshift. (9) Source of systemic redshift (MUSE EMission or ABSorption, KMOS, MOSFIRE). (10) Lyα velocity offset, $\Delta v(\mathrm{Ly}\alpha) = c(z_{\mathrm{Ly}\alpha}^{\mathrm{red}} - z_{\mathrm{sys}})/(1 + z_{\mathrm{sys}})$. (11) Stellar mass. (12) Star formation rate from MAGPHYS, with a minimum uncertainty of 0.1 dex.

[a] Blended with a $z = 0.83$ foreground object.

ORCID iDs

Leindert A. Boogaard https://orcid.org/0000-0002-3952-8588
Rychard J. Bouwens https://orcid.org/0000-0002-4989-2471
Dominik Riechers https://orcid.org/0000-0001-9585-1462
Paul van der Werf https://orcid.org/0000-0001-5434-5942
Jorryt Matthee https://orcid.org/0000-0003-2871-127X
Mauro Stefanon https://orcid.org/0000-0001-7768-5309
Anna Feltre https://orcid.org/0000-0001-6865-2871
Michael Maseda https://orcid.org/0000-0003-0695-4414
Hanae Inami https://orcid.org/0000-0003-4268-0393
Manuel Aravena https://orcid.org/0000-0002-6290-3198
Jarle Brinchmann https://orcid.org/0000-0003-4359-8797
Chris Carilli https://orcid.org/0000-0001-6647-3861
Thierry Contini https://orcid.org/0000-0003-0275-938X
Roberto Decarli https://orcid.org/0000-0002-2662-8803
Jorge González-López https://orcid.org/0000-0003-3926-1411
Themiya Nanayakkara https://orcid.org/0000-0003-2804-0648
Fabian Walter https://orcid.org/0000-0003-4793-7880

References

Akhlaghi, M., & Ichikawa, T. 2015, ApJS, 220, 1
Aravena, M., Boogaard, L., Gónzalez-López, J., et al. 2020, ApJ, 901, 79
Aravena, M., Decarli, R., Gónzalez-López, J., et al. 2019, ApJ, 882, 136
Asplund, M., Grevesse, N., Sauval, A. J., & Scott, P. 2009, ARA&A, 47, 481
Bacon, R., Conseil, S., Mary, D., et al. 2017, A&A, 608, A1
Baker, A. J., Tacconi, L. J., Genzel, R., Lehnert, M. D., & Lutz, D. 2004, ApJ, 604, 125
Bakx, T. J., Tamura, Y., Hashimoto, T., et al. 2020, MNRAS, 493, 4294
Béthermin, M., Fudamoto, Y., Ginolfi, M., et al. 2020, A&A, 643, A2
Bolatto, A. D., Wolfire, M., & Leroy, A. K. 2013, ARA&A, 51, 207
Boogaard, L. A., Decarli, R., González-López, J., et al. 2019, ApJ, 882, 140
Boogaard, L. A., van der Werf, P., Weiss, A., et al. 2020, ApJ, 902, 109
Bouwens, R. 2016, ApJ, 883, 72
Bouwens, R., González-López, J., Aravena, M., et al. 2020, ApJ, 902, 112
Bradač, M., Garcia-Appadoo, D., Huang, K. H., et al. 2017, ApJ, 836, L2
Brinchmann, J., Charlot, S., White, S. D. M., et al. 2004, MNRAS, 351, 1151
Brinchmann, J., Kunth, D., & Durret, F. 2008, A&A, 485, 657
Capak, P. L., Carilli, C., Jones, G., et al. 2015, Natur, 522, 455
Carilli, C. L., & Walter, F. 2013, ARA&A, 51, 105
Carniani, S., Maiolino, R., Amorin, R., et al. 2018b, MNRAS, 478, 1170
Carniani, S., Maiolino, R., Smit, R., & Amorín, R. 2018a, ApJ, 854, L7
Carniani, S., Ferrara, A., Maiolino, R., et al. 2020, MNRAS, 499, 5136
Cassata, P., Liu, D., Groves, B., et al. 2020, ApJ, 891, 83
Chabrier, G. 2003, PASP, 115, 763
Coogan, R. T., Sargent, M. T., Daddi, E., et al. 2019, MNRAS, 485, 2092
Coppin, K. E. K., Swinbank, A. M., Neri, R., et al. 2007, ApJ, 665, 936
Cormier, D., Abel, N. P., Hony, S., et al. 2019, A&A, 626, A23
Cormier, D., Madden, S. C., Lebouteiller, V., et al. 2015, A&A, 578, A53
Croxall, K. V., Smith, J. D., Pellegrini, E., et al. 2017, ApJ, 845, 96
Curti, M., Cresci, G., Mannucci, F., et al. 2017, MNRAS, 465, 1384
Da Cunha, E., Charlot, S., & Elbaz, D. 2008, MNRAS, 388, 1595
da Cunha, E., Groves, B., Walter, F., et al. 2013, ApJ, 766, 13
Da Cunha, E., Walter, F., Smail, I. R., et al. 2015, ApJ, 806, 110
Daddi, E., Bournaud, F., Walter, F., et al. 2010a, ApJ, 713, 686
Daddi, E., Dannerbauer, H., Liu, D., et al. 2015, A&A, 577, A46
Daddi, E., Elbaz, D., Walter, F., et al. 2010b, ApJ, 714, L118
Davies, R. I., Agudo Berbel, A., Wiezorrek, E., et al. 2013, A&A, 558, A56
Decarli, R., Aravena, M., Boogaard, L., et al. 2020, ApJ, 902, 110
Decarli, R., Walter, F., Gónzalez-López, J., et al. 2019, ApJ, 882, 138
Dessauges-Zavadsky, M., Ginolfi, M., Pozzi, F., et al. 2020, A&A, 643, A5
Dessauges-Zavadsky, M., Zamojski, M., Rujopakarn, W., et al. 2017, A&A, 605, A81
Dessauges-Zavadsky, M., Zamojski, M., Schaerer, D., et al. 2015, A&A, 577, A50
Díaz-Santos, T., Armus, L., Charmandaris, V., et al. 2017, ApJ, 846, 32
Draine, B. T., Dale, D. A., Bendo, G., et al. 2007, ApJ, 663, 866
Drake, A. B., Garel, T., Wisotzki, L., et al. 2017, A&A, 608, A6
Dunlop, J. S., McLure, R. J., Biggs, A. D., et al. 2017, MNRAS, 466, 861
Erb, D. K., Steidel, C. C., Shapley, A. E., et al. 2006, ApJ, 646, 107
Erb, D. K., Steidel, C. C., Trainor, R. F., et al. 2014, ApJ, 795, 33
Feltre, A., Maseda, M. V., Bacon, R., et al. 2020, A&A, 641, A118
Fletcher, T. J., Saintonge, A., Soares, P. S., & Pontzen, A. 2021, MNRAS, 501, 411
Franco, M., Elbaz, D., Zhou, L., et al. 2020, A&A, 643, A53
Geach, J. E., Smail, I., Moran, S. M., et al. 2011, ApJ, 730, L19
Genzel, R., Tacconi, L. J., Combes, F., et al. 2012, ApJ, 746, 69
Genzel, R., Tacconi, L. J., Gracia-Carpio, J., et al. 2010, MNRAS, 407, 2091
Genzel, R., Tacconi, L. J., Lutz, D., et al. 2015, ApJ, 800, 20
Gnedin, N. Y., & Draine, B. T. 2014, ApJ, 795, 4
González-López, J., Decarli, R., Pavesi, R., et al. 2019, ApJ, 882, 139
González-López, J., Novak, M., Decarli, R., et al. 2020, ApJ, 897, 91
Gowardhan, A., Riechers, D., Pavesi, R., et al. 2019, ApJ, 875, 6
Harikane, Y., Ouchi, M., Inoue, A. K., et al. 2020, ApJ, 896, 93
Hashimoto, T., Laporte, N., Mawatari, K., et al. 2018, Natur, 557, 392
Herenz, E. C., Wisotzki, L., Saust, R., et al. 2019, A&A, 621, A107
Hunt, L. K., García-Burillo, S., Casasola, V., et al. 2015, A&A, 583, A114
Hunter, J. D. 2007, CSE, 9, 90
Inami, H., Bacon, R., Brinchmann, J., et al. 2017, A&A, 608, A2
Inami, H., Decarli, R., Walter, F., et al. 2020, ApJ, 902, 113
Israel, F. 1997, A&A, 328, 471
Kewley, L. J., & Ellison, S. L. 2008, ApJ, 681, 1183
Knudsen, K. K., Richard, J., Kneib, J. P., et al. 2016, MNRAS Lett., 462, L6
Labbé, I., Bouwens, R., Illingworth, G. D., & Franx, M. 2006, ApJ, 649, L67
Labbé, I., Gonzlez, V., Bouwens, R. J., et al. 2010, ApJL, 708, 26
Labbé, I., Oesch, P. A., Illingworth, G. D., et al. 2015, ApJS, 221, 23
Laporte, N., Katz, H., Ellis, R. S., et al. 2019, MNRAS Lett., 487, L81
Le Fèvre, O., Béthermin, M., Faisst, A., et al. 2020, A&A, 643, A1
Lenkić, L., Bolatto, A. D., Förster Schreiber, N. M., et al. 2020, AJ, 159, 190
Leroy, A. K., Bolatto, A., Gordon, K., et al. 2011, ApJ, 737, 12
Li, A., & Draine, B. T. 2001, ApJ, 554, 778
Liu, D., Schinnerer, E., Groves, B., et al. 2019, ApJ, 887, 235
Livermore, R. C., Swinbank, A. M., Smail, I., et al. 2012, ApJL, 758, L35
Luo, B., Brandt, W. N., Xue, Y. Q., et al. 2017, ApJS, 228, 2
Madden, S. C., Cormier, D., Hony, S., et al. 2020, A&A, 643, A141
Magdis, G., Rigopoulou, D., Daddi, E., et al. 2017, A&A, 603, A93
Magdis, G. E., Daddi, E., Béthermin, M., et al. 2012, ApJ, 760, 6
Magnelli, B., Boogaard, L., Decarli, R., et al. 2020, ApJ, 892, 66
Magnelli, B., Lutz, D., Saintonge, A., et al. 2014, A&A, 561, A86
Maiolino, R., Carniani, S., Fontana, A., et al. 2015, MNRAS, 452, 54
Maiolino, R., Nagao, T., Grazian, A., et al. 2008, A&A, 488, 463
Maloney, P., & Black, J. H. 1988, ApJ, 325, 389
Mary, D., Bacon, R., Conseil, S., Piqueras, L., & Schutz, A. 2020, A&A, 635, A194
Matthee, J., Sobral, D., Boogaard, L. A., et al. 2019, ApJ, 881, 124
Matthee, J., Sobral, D., Boone, F., et al. 2017, ApJ, 851, 145
Matthee, J., Sobral, D., Oteo, I., et al. 2016, MNRAS, 458, 449
McMullin, J., Waters, B., Schiebel, D., Young, W., & Golap, K. 2007, in ASP Conf. Ser. 376, CASA Architecture and Applications, ed. R. Shaw, F. Hill, & D. Bell (San Francisco, CA: ASP), 127
Muzahid, S., Schaye, J., Marino, R. A., et al. 2020, MNRAS, 496, 1013
Newville, M., Otten, R., Nelson, A., et al. 2021, lmfit/lmfit-py v1.0.2., Zenodo, doi:10.5281/zenodo.4516651
Oke, J. B., & Gunn, J. E. 1983, ApJ, 266, 713
Ota, K., Walter, F., Ohta, K., et al. 2014, ApJ, 792, 34
Ouchi, M., Ellis, R., Ono, Y., et al. 2013, ApJ, 778, 102
Ouchi, M., Shimasaku, K., Akiyama, M., et al. 2008, ApJS, 176, 301
Papadopoulos, P. P., Thi, W. F., & Viti, S. 2004, MNRAS, 351, 147
Pavesi, R., Riechers, D. A., Capak, P. L., et al. 2016, ApJ, 832, 151
Pavesi, R., Riechers, D. A., Faisst, A. L., Stacey, G. J., & Capak, P. L. 2019, ApJ, 882, 168
Pentericci, L., Carniani, S., Castellano, M., et al. 2016, ApJ, 829, L11
Perez, F., & Granger, B. E. 2007, CSE, 9, 21
Pettini, M., & Pagel, B. E. J. 2004, MNRAS, 348, L59
Planck Collaboration, Abergel, A., Ade, P. A. R., et al. 2011, A&A, 536, A21
Planck Collaboration, Ade, P. A. R., Aghanim, N., et al. 2016, A&A, 594, A13
Popping, G., Somerville, R. S., & Galametz, M. 2017, MNRAS, 471, 3152
Rafelski, M., Teplitz, H. I., Gardner, J. P., et al. 2015, AJ, 150, 31
Rémy-Ruyer, A., Madden, S. C., Galliano, F., et al. 2014, A&A, 563, A31
Riechers, D. A., Boogaard, L. A., Decarli, R., et al. 2020, ApJ, 896, L21
Riechers, D. A., Carilli, C. L., Walter, F., & Momjian, E. 2010, ApJL, 724, L153

Riechers, D. A., Pavesi, R., Sharon, C. E., et al. 2019, ApJ, 872, 7
Rigby, J. R., Bayliss, M. B., Chisholm, J., et al. 2018, ApJ, 853, 87
Saintonge, A., Catinella, B., Tacconi, L. J., et al. 2017, ApJS, 233, 22
Saintonge, A., Lutz, D., Genzel, R., et al. 2013, ApJ, 778, 2
Sanders, R. L., Shapley, A. E., Reddy, N. A., et al. 2020, MNRAS, 491, 1427
Sandstrom, K. M., Leroy, A. K., Walter, F., et al. 2013, ApJ, 777, 5
Schinnerer, E., Groves, B., Sargent, M. T., et al. 2016, ApJ, 833, 112
Schruba, A., Leroy, A. K., Walter, F., et al. 2012, AJ, 143, 138
Scoville, N., Lee, N., Bout, P. V., et al. 2017, ApJ, 837, 150
Scoville, N., Sheth, K., Aussel, H., et al. 2016, ApJ, 820, 83
Shapley, a. E., Steidel, C. C., Pettini, M., & Adelberger, K. L. 2003, ApJ, 588, 65
Smit, R., Bouwens, R. J., Carniani, S., et al. 2018, Natur, 553, 179
Solomon, P. M., Downes, D., & Radford, S. J. E. 1992, ApJ, 398, L29
Spilker, J. S., Marrone, D. P., Aguirre, J. E., et al. 2014, ApJ, 785, 149
Strong, A., & Mattox, J. 1996, A&A, 308, L21
Tacconi, L. J., Genzel, R., Neri, R., et al. 2010, Natur, 463, 781
Tacconi, L. J., Genzel, R., Saintonge, A., et al. 2018, ApJ, 853, 179
Tacconi, L. J., Genzel, R., & Sternberg, A. 2020, ARA&A, 58, 157
Tacconi, L. J., Neri, R., Genzel, R., et al. 2013, ApJ, 768, 74
Tan, Q., Daddi, E., Sargent, M., et al. 2013, ApJ, 776, L24
Taylor, M. B. 2005, in ASP Conf. Ser. 347, Astronomical Data Analysis Software and Systems XIV (San Francisco, CA: ASP), 29
The Astropy Collaboration, Price-Whelan, A. M., Sipőcz, B. M., et al. 2018, AJ, 156, 123
The Astropy Collaboration, Robitaille, T. P., Tollerud, E. J., et al. 2013, A&A, 558, A33
Trainor, R. F., Steidel, C. C., Strom, A. L., & Rudie, G. C. 2015, ApJ, 809, 89
Tremonti, C. a., Heckman, T. M., Kauffmann, G., et al. 2004, ApJ, 613, 898
Valentino, F., Daddi, E., Puglisi, A., et al. 2020, A&A, 641, A155
Valentino, F., Magdis, G. E., Daddi, E., et al. 2018, ApJ, 869, 27
Van Der Walt, S., Colbert, S. C., & Varoquaux, G. 2011, CSE, 13, 22
van der Wel, A., Bell, E. F., Häussler, B., et al. 2012, ApJS, 203, 24
Verhamme, A., Garel, T., Ventou, E., et al. 2018, MNRAS Lett., 478, L60
Walter, F., Carilli, C., Neeleman, M., et al. 2020, ApJ, 902, 111
Walter, F., Decarli, R., Aravena, M., et al. 2016, ApJ, 833, 67
Walter, F., Weiß, A., Downes, D., Decarli, R., & Henkel, C. 2011, ApJ, 730, 18
Weiß, A., Downes, D., Henkel, C., & Walter, F. 2005, A&A, 429, L25
Weiß, A., Henkel, C., Downes, D., & Walter, F. 2003, A&A, 409, L41
Whitaker, K. E., Franx, M., Leja, J., et al. 2014, ApJ, 795, 104
Wolfire, M. G., Hollenbach, D., & McKee, C. F. 2010, ApJ, 716, 1191
Wuyts, E., Kurk, J., Förster Schreiber, N. M., et al. 2014, ApJL, 789, L40
Yang, H., Malhotra, S., Gronke, M., et al. 2017, ApJ, 844, 171
Zahid, H. J., Dima, G. I., Kudritzki, R.-P., et al. 2014, ApJ, 791, 130
Zanella, A., Daddi, E., Magdis, G., et al. 2018, MNRAS, 481, 1976